

Tissue shape determines actin-dependent nuclear migration mechanisms in neuroepithelia

Iskra Yanakieva¹, Anna Erzberger^{1,2}, Marija Matejčić¹, Carl D. Modes^{1,3} and Caren Norden^{1*}

¹ Max Planck Institute of Molecular Cell Biology and Genetics, Pfotenhauerstraße 108, 01307 Dresden, Germany

² Max Planck Institute for the Physics of Complex Systems, Nöthnitzer Straße 38, 01187 Dresden, Germany

³ Max Planck Center for Systems Biology, Pfotenhauerstraße 108, 01307 Dresden, Germany

* Corresponding Author:

Caren Norden (C.N.): norden@mpi-cbg.de

ABSTRACT

Correct nuclear position is crucial for cellular function. Depending on cell context however, cytoskeletal elements and force generation mechanisms vary. While these mechanisms have been intensely studied in single cells, how nuclear positioning is linked to tissue morphology is less clear. Here, we compare apical nuclear positioning in developing straight and curved neuroepithelia of zebrafish.

Interestingly, in differently shaped neuroepithelia the kinetics of nuclear positioning differ and we find that distinct actin-dependent mechanisms are employed. In straight neuroepithelia nuclear positioning is controlled by Rho-ROCK-dependent myosin contractility. Curved neuroepithelia use a formin-dependent pushing mechanism for which we propose a force generation theory.

We suggest that cytoskeleton adaptability to tissue shape ensures correct nuclear positioning and robust epithelial maturation across different geometries. We further speculate that different mechanisms arise due to differences in actin arrangements during development, a theme highlighting the importance of developmental context for the execution of intracellular processes.

INTRODUCTION

Nuclear position in cells can vary depending on type, cell cycle phase, migratory state or differentiation stage (Gundersen and Worman, 2013). As nuclear positioning is a prerequisite for the correct execution of crucial cellular programs including centered mitosis in fission yeast (Tran et al., 2001), differentiation of dermal cells in nematodes (Fridolfsson and Starr, 2010) or muscle cells in vertebrates (Roman and Gomes, 2018), and in neural system development (Shu et al., 2004; Tsai et al., 2007; Tsai and Gleeson, 2005), it needs to be tightly controlled. To ensure exact positioning within cells, nuclei are actively transported by cytoskeletal elements and both actin (Gomes et al., 2005; Luxton et al., 2010) and microtubules (Fridolfsson and Starr, 2010; Reinsch and Gonczy, 1998; Tran et al., 2001) can exert pulling or pushing forces on nuclei using a variety of mechanisms. Interestingly, even within a single cell type, like fibroblasts, the mechanisms of nuclear transport can vary depending on the context (Levy and Holzbaur, 2008; Petrie et al., 2014; Wu et al., 2014). This striking variety of mechanisms not only underlines the importance of nuclear position regulation, but also illustrates the adaptability of the cytoskeleton.

Diverse mechanisms of nuclear positioning have been studied extensively in cultured cells or the *C. elegans* zygote (Reinsch and Gonczy, 1998). However, how nuclear positioning is achieved in more complex contexts such as tissues within developing organisms is not well explored. In developing epithelia for example, complex and dynamic shape changes occur at the single cell level and at the tissue scale but it is not known how robust nuclear positioning is maintained across varying cell- and tissue geometries. Here, we address this question in pseudostratified neuroepithelia of the developing zebrafish. Pseudostratified neuroepithelia give rise to the nervous system, and correct nuclear positioning is crucial for their maturation. Nuclei in pseudostratified

neuroepithelia are densely-packed and occupy different apicobasal positions in interphase (Lee and Norden, 2013; Sauer, 1935) when nuclear movements are stochastic (Kosodo et al., 2011; Leung et al., 2011; Norden et al., 2009). Preceding mitosis, however, nuclei are actively moved to the apical surface (Kosodo et al., 2011; Leung et al., 2011; Norden et al., 2009) (Fig. 1 A). If nuclei fail to position apically, divisions occur at basal locations, which perturbs epithelial integrity and maturation (Strzyz et al., 2015). The cytoskeletal elements responsible for apical nuclear migration in neuroepithelia vary (Lee and Norden, 2013; Norden, 2017; Strzyz et al., 2016). In the rodent neocortex, movements are microtubule-dependent (Bertipaglia et al., 2017) and the mechanisms have been extensively studied (Hu et al., 2013; Shu et al., 2004; Tsai et al., 2010). In shorter neuroepithelia, however, nuclear positioning depends on the actin cytoskeleton (Strzyz et al., 2016) but it still is not fully understood how actin generates the forces required for apical nuclear movement. Rho-associated protein kinase (ROCK) has been implicated in apical nuclear migration (Meyer et al., 2011) in the *Drosophila* wing disc, but it is unclear whether this mechanism is conserved in all pseudostratified epithelia. Indications that nuclear positioning mechanisms in neuroepithelia might vary have come from a study of zebrafish retina and hindbrain (Leung et al., 2011). However, how mechanisms differ and whether differences are influenced by the tissue context has remained elusive. Furthermore, the effect of nuclear properties on neuroepithelial nuclear migration has not been addressed. Here, we investigate apical nuclear migration in zebrafish hindbrain and retinal neuroepithelia (Fig. 1 B, B') and find that strong nuclear deformability aids efficient apical migration. We further reveal differences in the nuclear kinetics between these tissues that result from different actin-dependent mechanisms: in the hindbrain the Rho-ROCK pathway is involved in apical nuclear migration, while in the retina nuclear movements are driven by an MLCK- and formin

activity-dependent mechanism. Furthermore, we show that other tissues, morphologically comparable to retina and hindbrain, exhibit similar apical migration modes implicating a relation between cell and tissue shape and nuclear positioning mechanisms.

RESULTS

Apical migration of retinal and hindbrain nuclei occurs with different kinetics

To understand the reported kinetic differences between apical nuclear migration in hindbrain and retinal neuroepithelia (Leung et al., 2011) (Fig. 1 B), we quantified nuclear movements in both tissues using light sheet fluorescent microscopy (LSFM) at sub-minute resolution (Icha et al., 2017) (Fig. 1 C). The G2 phase of the cell cycle, during which active nuclear migration occurs, was identified using a PCNA marker (Leung et al., 2011; Strzyz et al., 2015) (Fig. 1 C, Video 1). Nuclear trajectory analysis (Fig. 1 D) revealed that nuclei in the retina generally start G2 movements relatively close to the apical surface (Fig. 1 E) while the variance of starting points was greater in the hindbrain (Fig. 1 E, Table 1). Nevertheless, hindbrain nuclei spent less time in migration than retinal nuclei (Table 1) indicating more directed movements. Quantitative analysis of apical nuclear movements revealed that hindbrain nuclei indeed showed a higher average instantaneous velocity compared to retinal nuclei (Table 1). Directionality ratio (Fig. 1 F, Table 1) and mean squared displacement analysis (Fig. S1 A) confirmed the higher directionality of hindbrain nuclei (Table 1). Characterization of instantaneous velocity distributions showed that retinal nuclei more frequently undergo negative (basal) movements than hindbrain nuclei (Fig. 1 G). We further compared the kurtosis, a measure of the contribution of infrequent extreme deviations to the tails of the distribution. This showed that extreme deviations were more common in retina than in hindbrain (Table 1) suggesting that retinal nuclei move in a more saltatory manner than hindbrain nuclei.

Overall, this analysis shows that apical nuclear movements differ between hindbrain and retina. While nuclei in the hindbrain start migration from more variable apico-basal

positions and move towards the apical surface in a directed and smooth manner, nuclei in the retinal neuroepithelium start more apically, move slower and are less directed. This made us ask whether the nuclei of the different neuroepithelia themselves could have different properties.

Nuclear deformations during apical migration occur only in the retinal neuroepithelia

As high nuclear stiffness can affect cell migration kinetics (Harada et al., 2014), we hypothesized that nuclear stiffness differences could underlie the different migration kinetics observed. Nuclear stiffness depends predominantly on A-type lamins (Swift et al., 2013) and nuclei with high Lamin A/C content are stiffer than those with more Lamin B (Harada et al., 2014; Rowat et al., 2013). Thus, to investigate nuclear properties in hindbrain and retina, we assessed Lamin A/C and Lamin B1 in their nuclear envelopes. While Lamin B1 was evenly distributed at nuclear envelopes of both tissues (Fig. 2 A), Lamin A/C was absent (Fig. 2 A) (Lamin A/C control staining (Fig. S1 A)). This argued against stiffness differences and suggested that neither hindbrain nor retinal nuclei are very rigid. Live-imaging of nuclei expressing the nuclear envelope marker LAP2B corroborated this notion, revealing frequent deformations and dynamic indentations of nuclear envelopes (Fig. 2 B). Further, upon interference with neuroepithelial integrity by laser ablation, both retinal and hindbrain nuclei exhibited dramatic shape changes before recovering ellipsoidal shape (Fig. 2 C, Video 2). We speculated that this extreme nuclear deformability could aid nuclear movements through the crowded (Matejic et al., 2018) neuroepithelial environment. To test this idea, we overexpressed Lamin A (LmnA) in a subset of retinal nuclei (Fig. 2 D). These nuclei did not move apically as efficiently as

nuclei in controls and sometimes divided at sub-apical positions (Fig. 2 E, Video 3). This indicated that nuclear stiffness influences the efficiency of nuclear migration.

While these data showed that hindbrain and retinal nuclei have similarly low nuclear stiffness they did not explain the differing apical migration kinetics observed. We thus used nuclear deformations as a proxy for the forces that act on nuclei moving apically. 3D segmented nuclei were used to compare G2 to S phase shapes (Fig. 2 F). In S phase, nuclei in both hindbrain and retina showed elongated, ellipsoidal shapes (Fig. 2 F). During G2, no consistent changes were seen for nuclei in the hindbrain (Fig. 2 F) while retinal nuclei generally became more ovoid (Fig. 2 F). We quantified these shape changes by calculating the nuclear aspect ratio before and after migration onset. Both hindbrain and retinal nuclei showed periods of deformation and relaxation in S and G2 (Fig. S1 C) but only retinal nuclei showed an average aspect ratio increase (Fig. 2 G, Table 1). Cross-correlation demonstrated that the dynamics of retinal nuclear aspect ratio in G2 was positively correlated with the dynamics in instantaneous velocity (Fig. 2 H; Fig. S1 D). This suggests that retinal nuclei deform as a result of the forces that propel the nucleus apically.

In conclusion, low nuclear stiffness, due to the absence of Lamin A/C, can aid efficient nuclear movement in neuroepithelia. However, only retinal nuclei undergo consistent aspect ratio changes during movement. This, together with the observation that the kinetics of nuclear movements differ between the neuroepithelia, indicates that cytoskeletal forces act differently on hindbrain and retinal nuclei.

Distinct actomyosin pools are involved in nuclear movements in hindbrain and retina

The forces that drive apical nuclear migration in different pseudostratified epithelia can be generated by actomyosin (Meyer et al., 2011; Norden et al., 2009) or microtubules (Hu et al., 2013; Shu et al., 2004; Strzyz et al., 2016; Tsai et al., 2010). While it has been shown that in retinal neuroepithelia apical nuclear migration is actomyosin-dependent (Norden et al., 2009; Strzyz et al., 2015), the cytoskeletal elements that move nuclei in hindbrain neuroepithelia are unknown. We thus performed colcemid and blebbistatin treatment to interfere respectively with microtubule or actomyosin activity. We found that blebbistatin but not colcemid treatment impaired apical nuclear movement in hindbrain (Fig. S2 A) showing that nuclear migration is microtubule-independent but actomyosin-dependent, similar to the retina (Norden et al., 2009; Strzyz et al., 2015). The importance of the actin cytoskeleton to move nuclei apically in both tissues was confirmed by combined interference with actin polymerization using Latrunculin A, and actin turnover, using Jasplakinolide (Fig. S3 A).

As the same cytoskeletal elements drive nuclei to apical positions in retina and hindbrain, we hypothesized that actin itself acts differently on their nuclei. To test this idea, we imaged actin distribution during G2. In retinal cells actin was enriched within the cytoplasm basally to the nucleus and followed the nucleus during migration (Fig. 3 A, b, b', Video 4). In contrast, the actin signal in hindbrain cells was mainly localized to the cell periphery (Fig. 3 A, B', Video 4). Live imaging of myosin distribution confirmed cytoplasmic basal enrichment only in the retina (Fig. S2 B, Video 5). The actin 'cloud' following the nucleus in retinal cells had no persistent intensity but appeared to fluctuate with a similar frequency as the nuclear instantaneous velocity and the aspect ratio (Fig.

3 C, C', C'', D, Fig. S2C, Video 4), which was confirmed by cross-correlation analysis (Fig. 3 E). This suggests that basal actin enrichment is involved in the force-generation mechanism propelling the nucleus apically in the retina.

Together, this demonstrates that actin and myosin are the cytoskeletal elements driving apical nuclear migration in both hindbrain and retina. However, different actin pools act during apical nuclear migration in G2 of hindbrain and retinal cells.

Different actomyosin regulators control apical nuclear movements in hindbrain and retinal cells

We next investigated the actomyosin regulators that control the different actin pools in hindbrain and retina during apical nuclear movement. One regulatory pathway, previously suggested to be involved in apical nuclear migration in the *Drosophila* wing disk (Meyer et al., 2011), that controls both myosin activity and actin polymerization is the Rho-GTPase – ROCK pathway. We thus interfered with RhoA-GTPase or its effector ROCK, using respectively the small molecule inhibitors Rhosin, combined with Y16, (Fig. S3 B) and Rockout (Fig. 4 A, B). Compared to controls (Fig. 4 A, A', D), both treatments led to impaired apical nuclear movement in hindbrain. Some G2 nuclei never reached the apical surface, resulting in basal mitosis (Fig. 4 B, B', D, Video 6). Surprisingly, however, this was not the case in the retina. Here, nuclei moved similarly to controls (Fig. 4 B, B', D, Video 6). This was confirmed by overexpression of a dominant negative ROCK variant, DN-Rok2 (Marlow et al., 2002) (Fig. 4 F). Hence, apical migration in the hindbrain but not in the retina depends on ROCK-dependent activation of myosin.

Despite its independence of the Rho-GTPase – ROCK pathway, general myosin inhibition by blebbistatin stalls apical nuclear migration also in the retina (Norden et al., 2009). We therefore tested whether another common myosin activator, MLCK (Myosin

light-chain kinase), was involved in nuclear movements by interference with MLCK activity using the inhibitor ML-7 (Fig. S3 C). This treatment had no effect on apical nuclear migration in the hindbrain but led to basally stalled G2 nuclei in the retina (Fig. S3 C). As earlier studies showed that ROCK and MLCK can be involved in the formation and contractility of distinct pools of actin stress fibers (Totsukawa et al., 2000), we tested whether they might also regulate distinct actin pools in neuroepithelial progenitors and probed the role of different actin nucleators in the process. Inhibition of the Arp2/3 complex, responsible for branched actin nucleation, using CK-666 had no effect on apical nuclear migration in retinal or hindbrain neuroepithelia (Fig. S3 D), a result confirmed by overexpression of a dominant negative variant of the Arp2/3 activator NWASP (Icha et al., 2016a) (Fig. S4 A, B). Another major actin nucleator protein family are formins. Application of the pan-formin inhibitor SMIFH2 had no effect on nuclear migration in hindbrain (Fig. 4 C, C', E, Video 6). In contrast, nuclei in retinal tissues treated with SMIFH2 often stalled basally for hours or did not reach the apical surface at all (Fig. 4 C, C', E, Video 6).

As formins are a diverse protein family, we set out to identify the formins involved in nuclear migration in the retinal tissue. One suggestion came from a transcriptomics analysis (Sidhaye and Norden, GSE124779) that showed Fmnl3 (formin-like 3 protein) expression in the retina, which was confirmed by *in situ* hybridization (Fig. S4 C).

Expression of GFP-tagged Fmnl3 revealed that the protein forms patches localized predominantly at the cell cortex in retinal progenitors (Fig. 4 H, Video 8). During G2 these Fmnl3 patches showed enrichment 5 μ m - 10 μ m basally of the nucleus (Fig. 4 H, H') indicating that the observed actin 'cloud' basally to retinal nuclei (Fig. 3 A, B', C', C'') was nucleated by Fmnl3. Specific interference with Fmnl3 activity by overexpression of a dominant negative version, Fmnl3 Δ C (Phng et al., 2015), demonstrated that indeed

Fmn13 perturbation affected apical nuclear migration in retinal but not hindbrain tissue (Fig. 4 G, Video 7).

These results show that while actin is the main driver of apical nuclear migration in both neuroepithelia, different actomyosin regulators are at play (Fig. S3 E). In hindbrain apical nuclear movement depends on Rho-GTPase-ROCK while in the retina MLCK-dependent contractility and formin-dependent actin polymerization are involved.

Different actin-dependent mechanisms of apical nuclear migration are linked to different cell and tissue shape

Hindbrain and retinal neuroepithelia display a similar pseudostratified architecture at similar developmental stages in the same organism. Nevertheless, cells employ distinct actomyosin-dependent force generation mechanisms to move nuclei. It was hypothesized that tissue and cell parameters like length and morphology can influence the cytoskeletal mechanisms generating force for apical nuclear migration (Strzyz et al., 2016). We thus tested whether cell and tissue architecture could influence the force generation mechanism observed and analyzed tissue thickness, cell shape (Table 2), and tissue-wide actomyosin distribution in both neuroepithelia (Fig. 5 A, B). While tissue thickness was similar in retina and hindbrain (Table 2), cell shape differed. Hindbrain cells were cylindrical with comparable apical and basal cell surface area (Table 2), whereas retinal cells had a more conical shape with the cells' apical surface areas greater than basal surface areas (Table 2). Cell shape differences were reflected by different neuroepithelial geometry, a straight epithelium in hindbrain and a curved epithelium in the retina (Fig. 1 B, B', 5A). Hindbrain and retinal neuroepithelia also differed in tissue-wide distribution of actin, myosin and nuclei along the apicobasal axis. In hindbrain actin and myosin were evenly distributed along the lateral cell borders with

peak intensities at apical and basal surfaces and nuclei dispersed all along the apicobasal axis (Fig. 5 A, B). In retinal neuroepithelia a basal bias of actin and myosin ((Matejic et al., 2018; Sidhaye and Norden, 2017), Fig. 5 A, B), leading to the formation of a nuclear exclusion zone was observed (Fig. 5 B, (Matejic et al., 2018)).

To test whether these differences influence apical nuclear movements, we investigated the process in other straight and curved zebrafish neuroepithelia at the midbrain-hindbrain boundary (MHB). The MHB is curved at a point, termed MHBC (C for constriction (Gutzman et al., 2008) while its neighboring regions (referred to as MHBS) are straight at this developmental stage (Fig. 5 C). MHBS and MHBC had comparable thickness (Table 2). Shapes of MHBS cells were similar to those of hindbrain progenitors while MHBC cell shapes were similar to retinal progenitors (Table 2). Actomyosin and nuclear distribution in the MHBC matched the basal actin enrichment and the nuclear exclusion zone found in retinal tissue, while no basal accumulation was seen in the MHBS and nuclei, like in hindbrain, were positioned along the complete apico-basal axis (Fig. 5 D, E, Table 2).

We tested whether nuclear migration characteristics reflect the architectural similarities in the two curved and the two straight tissues. Indeed, nuclear trajectories in the two curved neuroepithelia (MHBC and retina) showed striking resemblance, as did the trajectories in the two straight neuroepithelia (MHBS and hindbrain) (Fig. 5 F). In agreement with this, G2 nuclei in MHBS moved faster than those in MHBC and mean instantaneous velocities between MHBS and hindbrain matched, as did velocities between MHBC and retina (Table 2). Furthermore, nuclear movements in MHBS showed a higher directionality ratio than in MHBC (Fig. 5 G, Table 2) and MHBC nuclei, like retinal nuclei, changed their aspect ratio during G2 while nuclear aspect ratio changed significantly less in MHBS cells (Fig. 5 H, Table 2). Live imaging of G2 actin

showed a 'cloud' of actin accumulation following the nucleus in MHBC, similarly to retinal cells (Fig. 5 I) while in MHBS cells actin remained cortical during apical movement, similar to hindbrain (Fig. 5 I).

We conclude that cell and tissue shape influence the actin-dependent mechanisms that move nuclei apically in similar tissues within the same organism. The fact that actin is differently regulated in differently shaped neuroepithelia to achieve the same goal stresses the robustness of apical nuclear migration and the adaptability of the cytoskeletal elements driving it.

DISCUSSION

Here, we show that the cytoskeletal force generating mechanisms for nuclear positioning can vary in similar tissues within the same organism depending on cell and tissue geometry. In particular, we found that apical nuclear migration in pseudostratified neuroepithelia of different curvature is driven by distinct actomyosin-dependent force generating mechanisms. We propose that an actomyosin contractility-dependent mechanism, downstream of the Rho-ROCK pathway, acts in the straight hindbrain tissue, while nuclei seem to be pushed by a formin-nucleated expanding actin network in the curved retinal tissue. Interestingly, in both tissues nuclei are unusually deformable and nuclear deformability aids efficient movements through the crowded neuroepithelia.

Extreme nuclear deformability as a prerequisite for movements within a crowded tissue

We showed that Lamin A/C, a major contributor to nuclear mechanical stiffness (Swift et al., 2013), is not expressed in nuclear envelopes of zebrafish neuroepithelial cells. These nuclei consequently display significant deformations. Overexpression of Lamin A/C hampers apical migration, indicating that nuclear deformability facilitates these movements. Similarly, nuclear deformability has been shown to be crucial for cell migration through pores with constraining size (Davidson et al., 2015; Harada et al., 2014; Rowat et al., 2013; Wolf et al., 2013). Future studies should investigate whether the observed deformability of nuclei in neuroepithelia helps the complex nuclear migration phenomena occurring during the proliferative growth phase in these tissues.

Possible mechanisms of apical nuclear migration

Apical nuclear migration in hindbrain cells depends on ROCK activity with actin enriched at the cell periphery. ROCK-dependent cortical contractility was previously implicated in apical nuclear migration in *Drosophila* wing disc (Meyer et al., 2011). One possible contractility-dependent mechanism is the generation of cortical flows, similarly to those in *C. elegans* zygotes or cells undergoing adhesion-free migration (Bergert et al., 2015; Mayer et al., 2010; Munro et al., 2004). Gradual contraction of the cortex due to the action of a multitude of myosin motors could further explain the faster and smoother nuclear migration in hindbrain. Future experiments, including specific perturbation of cortical contractility, will help to test this hypothesis.

In the retina, basal enrichment of actin and myosin in G2 was reported previously (Leung et al., 2011; Norden et al., 2009) and it was proposed that nuclei are propelled by basal process constriction. However, we did not observe such constriction during apical migration of retinal nuclei (Fig. 1 C, 3 A). In contrast, the periodic enrichment of actomyosin that closely follows nuclei during movement and the accompanying nuclear deformations argue that an expanding actin network pushes the nucleus apically. Polymerizing actin networks were shown to generate saltatory movements *in vitro* (Delatour et al., 2008), in the motility of intracellular parasites (Gerbál et al., 2000; Soo and Theriot, 2005) and during the pushing of chromosomes in mouse oocytes (Li et al., 2008; Yi et al., 2013). The dependence of retinal apical migration on formin activity and the basal localization of Fmn13 beneath this network further argue for such a mechanism. MLCK-dependent myosin activity could help to crosslink (Murrell and Gardel, 2012; Thoresen et al., 2011; Thoresen et al., 2013) and organize actin filaments and provide increased stiffness of the network. A simple proof-of-principle mathematical model (Supplemental Material & Fig. 6 A) demonstrates that cortex-anchored bundled f-

actin can explain the observed phenomena. Cell geometry can direct f-actin growth, with frustum-shaped cells preferentially growing f-actin into the cytoplasm directed toward the larger side (Reymann et al., 2010). Thus, actin bundles growing via formin-catalyzed polymerization at the anchored end could push the nucleus toward the apical side by direct contact against the nuclear envelope. Intriguingly, the model shows that for appropriate parameter ranges the critical length for Euler buckling of the bundle (Bathe et al., 2008; Kierfeld et al., 2006) is consistent with the observed trailing distance of the formin enrichment zone behind the nucleus (Supplemental Material). Further, as the nucleus encounters spatial constraints, the effective dynamic viscosity would rise, resulting in a decreased buckling length threshold. As filaments then buckle, the continued addition of actin monomers at the trailing formin sites provide increased forces to the nucleus due to the rising stresses in the filaments, eventually squeezing the nucleus through. The buckled filaments and bundles then straighten, leading to a burst of increased velocity. A key prediction of this proof-of-principle model is that the average velocity of the nucleus is dominated by the speed of formin-catalyzed f-actin polymerization. Indeed, we observe that these are in close concert (Table 1, Fig. 1 G, Supplemental Material). The possibility that the coordinated expansion of the actin network pushes the nucleus apically is an exciting new mechanism for positioning nuclei that requires further exploration.

Cytoskeleton adaptability to tissue geometry ensures robust apical nuclear migration

Our finding that neuroepithelial cells in tissues with different curvature use distinct actin-dependent mechanisms for apical nuclear movements demonstrates the adaptability of the cytoskeleton when performing a task critical for cell function and tissue development.

Interestingly, actomyosin is responsible for both cell and tissue shape generation and maintenance, as well as the generation of the intracellular forces during nuclear positioning. Hindbrain and retinal neuroepithelia differ in cell and tissue shape, as well as tissue-wide cytoskeleton organization (Fig. 5 A, B, (Matejcic et al., 2018; Sidhaye and Norden, 2017)). It is tempting to speculate that intracellular actin distribution, related to tissue shape, influences the force generation mechanism for apical nuclear migration. The tissue-wide basal enrichment of actomyosin, involved in curvature formation in the retina (Nicolas-Perez et al., 2016; Sidhaye and Norden, 2017) could favor the formation of the basal structures that push the nucleus apically (Fig. 6 B). However, such a mechanism is only efficient in curved tissues with a basal actomyosin bias. Such bias is absent in the hindbrain where a different mechanism is employed (Fig. 6 B). To probe whether and how the cytoskeleton adapts to other spatial constraints, more studies of apical migration in other epithelial architecture regimes are needed, for example in apically constricted hindbrain regions, or during tissue thickening, as in the retinal neuroepithelium later in development (Matejcic et al., 2018). Apical migration is a prerequisite for apical mitosis and, hence, correct tissue development in all pseudostratified epithelia. As these tissues are the precursors of many organs of diverse organisms (Norden, 2017), strong cytoskeletal adaptability is most likely crucial for successful development. The variety of described mechanisms of apical nuclear migration across different systems suggests that, for pseudostratified epithelial cells, this important end justifies the many means.

Materials and Methods

Zebrafish husbandry

Wild type zebrafish were maintained and bred at 26°C. Embryos were raised at 21, 28.5, or 32°C in E3 medium. Animals were staged in hpf (hours post fertilization) according to (Kimmel et al., 1995). From 8 hpf the medium was supplemented with 0.2 mM 1-phenyl-2-thiourea (PTU) (Sigma-Aldrich) to prevent pigmentation. Embryos were anaesthetized in 0.04% tricaine methanesulfonate (MS-222; Sigma-Aldrich) prior to live imaging. Live imaging was performed for 6-14 hours from 18 hpf for the hindbrain and MHB, and from 24 hpf for the retina. All animal work was performed in accordance with EU directive 2010/63/EU, as well as the German Animal Welfare Act.

RNA and DNA injections

To mosaically label cells in zebrafish neuroepithelia, DNA constructs were injected into one-cell stage embryos while mRNA was injected into the cytoplasm of a single blastomere of 32 - 128 cell stage embryos. DNA was injected at 10-25 pg per embryo. mRNA was synthesized using the Ambion mMessage mMachine kit and injected at 40 to 100 pg per embryo. The injection mix was prepared in water and the injected volume was 0.5-1.0 nl. A full list of the constructs used can be found in Table S1.

Cloning strategies

Gateway cloning (Thermo Fisher Scientific) based on the Tol2 kit (Kwan et al., 2007) was used for all constructs.

pCS2+ mKate2-PCNA

Human PCNA coding sequence was amplified from pCS2+ GFP-PCNA (Leung et al., 2011) and a 3'-entry clone was generated. It was combined with mKate2 p5ENTR(L1-L2) (kind gift from Andrew Oates) and pCS2+ pDEST(R1-R3) (Villefranc et al., 2007).

T2-hsp70: EGFP-LAP2b

Rat LAP2b coding sequence was amplified from a pmRFP_LAP2beta_IRES_puro2b plasmid (Steigemann et al., 2009), Addgene, 21047) and a 3'-entry clone was generated. It was combined with hsp70 promoter p5ENTR(L4-R1) clone (Kwan et al., 2007), EGFP pMENTR(L1-L2) (Villefranc et al., 2007) and GW Tol2-pA2 p DEST backbone (Villefranc et al., 2007).

T2-hsp70: LMNA-mKate2

RNA was extracted from 24 hpf embryos using the TRI Reagent (Sigma-Aldrich) according to the manufacturers protocol. cDNA was synthesized using first strand cDNA synthesis kit (Fermentas/ Thermo-Fischer scientific). Zebrafish lamin A (BC163807.1) coding sequence was amplified from zebrafish cDNA to generate a middle entry clone without a stop codon at the end. The following primers were used:

5' ggggacaagttgtacaaaaaagcaggctggGAGTCGCAGCACACTCTTT 3'

5' ggggaccactttgtacaagaaagctgggtcAATAGAGCAGTTGTCCACTTTGG 3'

It was combined with hsp70 promoter p5ENTR(L4-R1) clone (Kwan et al., 2007), mKate2 p3ENTR(R2-L3) (kind gift from Andrew Oates) and GW Tol2-pA2 p DEST backbone (Villefranc et al., 2007).

T2-hsp70: Fmnl3 Δ C-EGFP

The middle entry clone for truncated Fmnl3, lacking catalytic C terminus FH1, FH2, and DAD domains (pME-Fmnl3 Δ C) (Phng et al., 2015) was a kind gift from Li-Kun Phng. It was combined with hsp70 promoter p5ENTR(L4-R1) clone (Kwan et al., 2007), EGFP p3ENTR(R2-L3) (Villefranc et al., 2007) and GW Tol2-pA2 p DEST backbone (Villefranc et al., 2007).

T2-hsp70: Fmnl3-EGFP

Zebrafish Fmnl3 (NM_001346154) coding sequence was amplified from zebrafish cDNA to generate a middle entry clone without a stop codon at the end. The following primers were used:

5' ggggacaagttgtacaaaaaagcaggctggATGGGGAATATTGAGAGTGTGG 3'

5' ggggaccactttgtacaagaaagctgggtcGCAGATGGACTCGTCGAAGA 3'

It was combined with hsp70 promoter p5ENTR(L4-R1) clone (Kwan et al., 2007), mKate2 p3ENTR(R2-L3) (kind gift from Andrew Oates) and GW Tol2-pA2 p DEST backbone (Villefranc et al., 2007).

T2-hsp70: DN-Rok2-EGFP

The DN-Rok2 (Marlow et al., 2002) sequence was amplified to generate a middle entry clone. It was combined with hsp70 promoter p5ENTR(L4-R1) clone (Kwan et al., 2007), mKate2 p3ENTR(R2-L3) (kind gift from Andrew Oates) and GW Tol2-pA2 p DEST backbone (Villefranc et al., 2007).

Heat shock of embryos

To induce expression of the heat shock promoter (hsp70) - driven constructs, embryos were incubated in a water bath at 17 hpf for imaging the hindbrain and at 23 hpf for imaging the retina to induce expression. The heat shock lasted 20 min at 37°C for Hsp70: DN-Rok2-EGFP and 30 min at 39°C for Hsp70: NWASP-CA- mKate2 and Hsp70:Fmnl3-EGFP. For induction of Hsp70:Fmnl3 Δ C-EGFP, heat shocked lasted 15 minutes at 39°C for imaging the hindbrain neuroepithelium and for 20 minutes at 39°C when imaging the retinal neuroepithelium.

Drug treatments

All inhibitors were dissolved in DMSO, except Latrunculin A, that was dissolved in ethanol. Equal volumes of DMSO or ethanol as the stock inhibitor solution were used for control treatments. Dechorionated embryos were treated by incubation in E3 medium containing the inhibitors at their respective working concentrations (Table S2), either in plastic multi-well plates or in compartmentalized 35-mm glass bottom Petri dishes (Greiner Bio-One). All treatments were started after 17 hpf for the hindbrain and after 23 hpf for the retina.

Myosin perturbation for fixed imaging

Before fixation, embryos were incubated 6 h in DMSO, 125 μ M Rockout, and 100 μ M ML-7, and for 3 h in 100 μ M Blebbistatin.

Live imaging of chemical perturbations

Embryos were dechorionated and pre-treated for one hour prior to mounting the sample. Concentrations for pre-treatment were 100 μ M Rhosin, 25 μ M Y16, 100 μ M Rockout, 200 μ M ML-7, 175 μ M CK-666, and 10 μ M SMIFH2. After mounting in agarose in glass-

bottom dishes, embryos were incubated in inhibitor concentrations listed in (Table S2) for 14 hours and imaged using a spinning disk confocal microscope.

Cells that completed S phase were counted using the CellCounter plugin in Fiji (Schindelin et al., 2012). Only embryos in which the drugs had an effect were analyzed. The numbers of treated and affected embryos are found in Table S3. Representative trajectories for controls, Rockout- and SMIFH2-treated cells were generated using the MTrackJ Fiji plugin.

Immunofluorescence

For wholemount immunostainings embryos were fixed in 4% paraformaldehyde (PFA) (Sigma) in PBS for actomyosin and nuclear imaging, and Dent's fixative for lamin immunostaining. The following antibodies and probes were used: Primary antibodies: 1:50 anti-phospho-myosin (Cell signaling), 1:500 anti-pH3 (Abcam), 1:200 anti-Lamin A/C (Abcam), 1:200 anti-Lamin B1 (Abcam). Secondary antibodies and fluorescent markers: 1:500 Alexa Fluor 647 anti-rat (Invitrogen), 1:500 Alexa Fluor 488 anti-Rabbit (Invitrogen), 1:500 Alexa Fluor 488 anti-mouse (Invitrogen), 1:500 Alexa Fluor 594 anti-Rabbit (Thermo Fischer Scientific), 1:50 Alexa Fluor 488 Phalloidin (Molecular Probes), 1:50 Rhodamine-Phalloidin (Molecular probes), DAPI.

Microscope image acquisition

Experiments in the hindbrain were conducted between 18 hpf and 30 hpf, and between 24 hpf and 36 hpf in the retina before full onset of neurogenesis for each tissue.

Confocal scans

Fixed samples were imaged in Zeiss LSM 880 inverted point scanning confocal system (Carl Zeiss Microscopy) using the 40x/1.2 C-Apochromat water immersion objective (Carl Zeiss Microscopy). Samples were mounted in 1% agarose in glass bottom dishes (MatTek) or compartmentalized glass bottom dishes (Greiner Bio-One) filled with PBS and imaged at room temperature. z-stacks acquired had a thickness of 20-36 μm and step size of 0.75-1 μm . The microscope was operated by ZEN 2 (black edition) software.

Time-lapse imaging using spinning disk confocal microscope (SDCM)

Live imaging of apical migration perturbations was done using an Andor SDCM system. The spinning disk setup consisted of IX71 microscope (Olympus) and CSU-X1 scan head (Yokogawa). The samples were mounted in compartmentalized glass bottom dishes (Greiner Bio-One) or glass bottom dishes (MatTek) into 0.9% agarose in E3 medium containing 0.1 M HEPES pH=7.25 and 0.01% MS-222 (Sigma). The dish was filled with E3 medium containing 0.01% MS-222 (Sigma). Imaging was performed with UPLSAPO 60x/1.5 water immersion objective (Olympus) and Neo sCMOS camera (Andor) at 28.5°C regulated by an environmental chamber. A z stack of thickness 35-36 μm was acquired with 1 μm steps. Images were taken every 5 - 7 min for 12 - 14 hours. The microscope was operated by Andor iQ 3.0 software.

Time-lapse imaging using light-sheet fluorescent microscope (LSFM)

Imaging of single labelled cells in the hindbrain, retina, and MHB, was performed as previously described (Icha et al., 2016b) using the Lightsheet Z.1 (Carl Zeiss Microscopy). The sample chamber was filled with E3 medium containing 0.01% MS-222 (Sigma) and 0.2 mM N-Phenylthiourea (Sigma) and maintained at 28.5°C. The embryos

were embedded in a 0.9% agarose column and a 25 - 35 μm z stack of the hindbrain, retina, or MHB was acquired with 1 μm steps in a single view, single-sided illumination mode. Images were taken every 0,25 -1 min for 3 - 4 hours using the Plan-Apochromat 40x/1.0 W detection objective (Carl Zeiss Microscopy) and the two PCO.Edge 5.5 sCMOS cameras. The microscope was operated by ZEN 2014 (black edition) software.

Laser ablations

Laser ablations were performed using an Andor SDCM system using an ultraviolet laser (MicroPoint unit), focused by 60x/1.25 water immersion objective (Olympus). A linear region of interest was defined in order to sever the apical or basal processes of neuroepithelial cells and cause perturbation to the structure of the neuroepithelium. Nuclei were visualized using the chromatin marker H2B-RFP. 16 z-planes spanning 12 μm of the tissue surrounding the region of interest were acquired prior to ablation during 3 time points 10 seconds apart. 20 repeats with a frequency of 30 Hz of the laser pulse were performed on the linear region of interest. 16 z-planes spanning 12 μm of the tissue surrounding the cut were scanned for 1 - 5 minutes with temporal resolution of 10 seconds to record the deformations of nuclei in the hindbrain and the retina after the cut.

***In situ* hybridization**

Riboprobes were generated from cDNA templates and in situ hybridization was performed as previously described (Oates and Ho, 2002; Thisse et al., 1993). The following primers were used to generate the probes for *Fmnl3* (lowercase bases contain T7 polymerase promoter):

Probe 1 5' ATCACATAGGGTGGGTTCGC 3'

 5' TAATACGACTCACTATAGGGATGACTGCCAGCTCCTTGTC 3'

Probe 2 5' GAGCAAGGTCTCCCAGAAGG 3'
 5' TAATACGACTCACTATAGGGATTGTTAAAGGCCTCCTCCGC 3'
Sense probe 5' ATTGTTAAAGGCCTCCTCCGC 3'
 5' TAATACGACTCACTATAGGGGAGCAAGGTCTCCCAGAAGG 3'

Wholemount stained embryos were documented using a Olympus SZX12 stereomicroscope equipped with a QImaging Micropublisher 5.0 RTV camera (QImaging).

Image analysis

Minimal image processing was used, prior to image analysis. Processing consisted of image cropping in ZEN and/ or Fiji (Schindelin et al., 2012), bleach correction and/ or background subtraction, as well as drift correction, using Fiji. After image analysis in Imaris 8 or 9 (BitPlane) or Fiji, data was analyzed and plotted using Microsoft Excel and GraphPad Prism. Statistical analysis was performed using GraphPad Prism.

Sample drift correction

Sample drift in 3D stacks was corrected using a Fiji plugin, created by Benoit Lombardot (Scientific Computing Facility, MPI-CBG, Dresden). The script can be found on http://imagej.net/Manual_drift_correction_plugin.

Analysis of apical nuclear migration kinetics

Beginning of G2 was defined by the disappearance of PCNA foci, indicating the end of S phase, until the onset of cell rounding (Leung et al., 2011). Apical migration was defined by the beginning of directed motion of the nucleus towards the apical side after the onset of G2 and before the onset of cell rounding.

To generate cell trajectories for instantaneous velocities, MSD, and directionality ratio analysis, nuclei were tracked in 3D using Imaris 8 or 9 (Bitplane) during S - phase and G2 - phase. Data points were taken at 1 min intervals. The cell axis was defined by the positions of the apical and basal endpoints, measured in 3D in the last time point of S phase for each cell. Nuclear position was projected onto the cell axis, obtaining one-dimensional time-series, as described (Leung et al., 2011). Resulting trajectories were analyzed as described previously (Leung et al., 2011). This analysis was performed using a custom MATLAB script. The kurtosis of instantaneous velocity distributions was calculated using GraphPad Prism.

Nuclear segmentation, shape measurements, and tracking in 3D

Semi-automatic segmentation and tracking were performed on 3D stacks in time-series of single labelled migrating nuclei using the Surface tool in Imaris 8 or 9 (Bitplane). The position of the nuclear centroid over time in 3D was extracted. In addition, an ellipsoid was fitted in the segmented surface in each timepoint by the software enabling the extraction of the length of the semi-axes of the nucleus. The nuclear aspect ratio A/C was calculated by dividing the length of each of one of the short semi-axes by the length of the long semi-axis, C .

The average nuclear aspect ratio during S phase was calculated for each nucleus (A/C_0) and used to calculate the value of the normalised aspect ratio for each timepoint in G2 (A/C_{norm_i}) following the formula:

$$A/C_{norm_i} = \frac{A/C_i - A/C_0}{A/C_0},$$

where A/C_i is the nuclear aspect ratio measured in each timepoint (t_i).

Normalized aspect ratios for each time point were pooled for all cells originating from the same tissue.

Tissue and cell shape measurements

Single cell length measurement in 3D

The 3D viewer of Imaris 8 or 9 (Bitplane) was used to visualize labelled cells in 3D. The positions of the edges of the apical and basal surface were defined using the Measurement Point tool in the last timepoint of S phase prior to the onset of migration. A custom MATLAB script was used to calculate the distance between the apical and basal surface of each cell and this distance was taken as the length of the cell.

Measurement of apical and basal cell footprint areas

Apical and basal cell footprints were segmented semi-automatically in Fiji. Linear regions of interest covering respectively the apical and basal footprint of S-phase cells were drawn to reslice the 3D stack and generate 2D stacks of the cell endfeet of at least 4 timepoints, 1 min apart. The footprints were segmented using automatic thresholding (Huang and Wang, 1995) using the stack histogram, selections were created, and their area measured every minute for 4-10 minutes.

Quantifications of actin distribution

Tissue-wide actin, myosin, and nuclear distribution profiles

The average fluorescent intensity distribution of phalloidin, phospho-myosin, and DAPI along the apico-basal cell axis was measured as described in (Matejic et al., 2018; Sidhaye and Norden, 2017). Regions of interest were defined as a 10 μm x 10 μm x (tissue thickness) cuboid for retina and hindbrain and 5 μm x 5 μm x (tissue thickness)

cuboid for MHBS and MHBC. 6 to 10 profiles originating from 4-6 samples were measured from each tissue.

Actin distribution profiles basally of the nucleus

Basal nuclear actin distribution profiles in hindbrain and retinal cells were measured in Fiji using region of interest immediately basally of the nucleus in each time point. The actin signal intensity in the central z-plane of the cell was measured and normalized to the minimum and the maximum for a given timepoint. The profiles from all timepoints in G2 were used to calculate the average actin profile for the hindbrain and retinal cells.

Analysis of basal actin oscillations and cross-correlation analysis

Average basal actin intensity was measured in a square region of interest in the SUM projection of each retinal cell for the duration of G2 using Fiji. Average actin intensity was normalized to the total actin signal in the cell for each timepoint. Data points were taken at intervals of 0.5 min. The peaks and plateaus in actin signal, instantaneous velocity, and nuclear aspect ratio were detected semi-automatically and their frequency was calculated using a custom MATLAB script. The fluctuations of basal actin were cross-correlated with the fluctuations of mean instantaneous velocity and normalized aspect ratio in MATLAB. Cross-correlation was computed on normalized data (area under curve was set to 1 and cross-correlation at minimal lag set to 1) in order to compare cross-correlation values between different cell parameters (fluorescence intensity, velocity, aspect ratio).

Statistical analysis

Statistical tests and definitions of error bars are indicated in the figure legends. All statistical tests were two sided. P values > 0.05 were considered not significant. All P values are indicated in the corresponding figure legends. Sample sizes are listed in Tables S3, S4, S5. Statistical analyses were performed using Prism 7 (GraphPad) software.

ACKNOWLEDGEMENTS

We thank the Norden lab, J. Brugués, S. Grill and especially G. Salbreux for fruitful project discussion. N. Kirkland, YL. Mao and P. Strzyz are thanked for helpful comments on the manuscript. We are grateful to H. Hollak, G. Jurado, S. Kaufmann, J. Sidhaye, the Light Microscopy Facility, Scientific Computing and the Fish Facility of the MPI-CBG for experimental help. We thank Li-Kun Phng for sharing the Fmnl3 Δ C construct.

I.Y. was a member of the IMPRS of Cell, Developmental and Systems Biology and recipient of an ELBE PhD fellowship. C.N. was supported by MPI-CBG and the German Research Foundation (NO 1068/1-1).

Author contributions

C. Norden and I. Yanakieva conceptualized and decided on methodology used in this work. I. Yanakieva performed majority of experiments and analysis. M.M. helped with experiments and analysis. A.E. designed analysis tools and performed analysis. C.M. generated the model. C.N. and I.Y. wrote the manuscript with help of all other authors.

Competing interests

The authors declare no competing financial interests.

References

- Bathe, M., C. Heussinger, M.M. Claessens, A.R. Bausch, and E. Frey. 2008. Cytoskeletal bundle mechanics. *Biophysical journal*. 94:2955-2964.
- Bergert, M., A. Erzberger, R.A. Desai, I.M. Aspalter, A.C. Oates, G. Charras, G. Salbreux, and E.K. Paluch. 2015. Force transmission during adhesion-independent migration. *Nature cell biology*. 17:524-529.
- Bertipaglia, C., J.C. Goncalves, and R.B. Vallee. 2017. Nuclear migration in mammalian brain development. *Seminars in cell & developmental biology*.
- Davidson, P.M., J. Sliz, P. Isermann, C. Denais, and J. Lammerding. 2015. Design of a microfluidic device to quantify dynamic intra-nuclear deformation during cell migration through confining environments. *Integrative biology : quantitative biosciences from nano to macro*. 7:1534-1546.
- Delatour, V., E. Helfer, D. Didry, K.H. Le, J.F. Gaucher, M.F. Carlier, and G. Romet-Lemonne. 2008. Arp2/3 controls the motile behavior of N-WASP-functionalized GUVs and modulates N-WASP surface distribution by mediating transient links with actin filaments. *Biophysical journal*. 94:4890-4905.
- Fridolfsson, H.N., and D.A. Starr. 2010. Kinesin-1 and dynein at the nuclear envelope mediate the bidirectional migrations of nuclei. *The Journal of cell biology*. 191:115-128.
- Gerbal, F., P. Chaikin, Y. Rabin, and J. Prost. 2000. An elastic analysis of Listeria monocytogenes propulsion. *Biophysical journal*. 79:2259-2275.
- Gomes, E.R., S. Jani, and G.G. Gundersen. 2005. Nuclear Movement Regulated by Cdc42, MRCK, Myosin, and Actin Flow Establishes MTOC Polarization in Migrating Cells. *Cell*. 121:451-463.
- Gundersen, G.G., and H.J. Worman. 2013. Nuclear positioning. *Cell*. 152:1376-1389.
- Gutzman, J.H., E.G. Graeden, L.A. Lowery, H.S. Holley, and H. Sive. 2008. Formation of the zebrafish midbrain-hindbrain boundary constriction requires laminin-dependent basal constriction. *Mechanisms of development*. 125:974-983.
- Harada, T., J. Swift, J. Irianto, J.-W. Shin, K.R. Spinler, A. Athirasala, R. Diegmiller, P.C.D.P. Dingal, I.L. Ivanovska, and D.E. Discher. 2014. Nuclear lamin stiffness is a barrier to 3D migration, but softness can limit survival. *The Journal of cell biology*. 204:669-682.
- Hu, D.J., A.D. Baffet, T. Nayak, A. Akhmanova, V. Doye, and R.B. Vallee. 2013. Dynein recruitment to nuclear pores activates apical nuclear migration and mitotic entry in brain progenitor cells. *Cell*. 154:1300-1313.
- Huang, L.-K., and M.-J.J. Wang. 1995. Image thresholding by minimizing the measures of fuzziness. *Pattern Recognition*. 28:41-51.
- Icha, J., C. Kunath, M. Rocha-Martins, and C. Norden. 2016a. Independent modes of ganglion cell translocation ensure correct lamination of the zebrafish retina. *The Journal of cell biology*. 215:259-275.
- Icha, J., C. Schmied, J. Sidhaye, P. Tomancak, S. Preibisch, and C. Norden. 2016b. Using Light Sheet Fluorescence Microscopy to Image Zebrafish Eye Development. *Journal of visualized experiments : JoVE*:e53966.
- Icha, J., M. Weber, J.C. Waters, and C. Norden. 2017. Phototoxicity in live fluorescence microscopy, and how to avoid it. *BioEssays : news and reviews in molecular, cellular and developmental biology*. 39.

- Kierfeld, J., P. Gutjahr, T. Kühne, P. Kraikivski, and R. Lipowsky. 2006. Buckling, Bundling, and Pattern Formation: From Semi-Flexible Polymers to Assemblies of Interacting Filaments. *Journal of Computational and Theoretical Nanoscience*. 3:898-911.
- Kimmel, C.B., W.W. Ballard, S.R. Kimmel, B. Ullmann, and T.F. Schilling. 1995. Stages of embryonic development of the zebrafish. *Developmental dynamics : an official publication of the American Association of Anatomists*. 203:253-310.
- Kosodo, Y., T. Suetsugu, M. Suda, Y. Mimori-Kiyosue, K. Toida, S.A. Baba, A. Kimura, and F. Matsuzaki. 2011. Regulation of interkinetic nuclear migration by cell cycle-coupled active and passive mechanisms in the developing brain. *The EMBO journal*. 30:1690-1704.
- Kwan, K.M., E. Fujimoto, C. Grabher, B.D. Mangum, M.E. Hardy, D.S. Campbell, J.M. Parant, H.J. Yost, J.P. Kanki, and C.B. Chien. 2007. The Tol2kit: a multisite gateway-based construction kit for Tol2 transposon transgenesis constructs. *Developmental dynamics : an official publication of the American Association of Anatomists*. 236:3088-3099.
- Lee, H.O., and C. Norden. 2013. Mechanisms controlling arrangements and movements of nuclei in pseudostratified epithelia. *Trends Cell Biol*. 23:141-150.
- Leung, L., A.V. Klopper, S.W. Grill, W.A. Harris, and C. Norden. 2011. Apical migration of nuclei during G2 is a prerequisite for all nuclear motion in zebrafish neuroepithelia. *Development (Cambridge, England)*. 138:5003-5013.
- Levy, J.R., and E.L. Holzbaur. 2008. Dynein drives nuclear rotation during forward progression of motile fibroblasts. *Journal of cell science*. 121:3187-3195.
- Li, H., F. Guo, B. Rubinstein, and R. Li. 2008. Actin-driven chromosomal motility leads to symmetry breaking in mammalian meiotic oocytes. *Nature cell biology*. 10:1301-1308.
- Luxton, G.W.G., E.R. Gomes, E.S. Folker, E. Vintinner, and G.G. Gundersen. 2010. Linear Arrays of Nuclear Envelope Proteins Harness Retrograde Actin Flow for Nuclear Movement. *Science (New York, N.Y.)*. 329:956-959.
- Marlow, F., J. Topczewski, D. Sepich, and L. Solnica-Krezel. 2002. Zebrafish Rho Kinase 2 Acts Downstream of Wnt11 to Mediate Cell Polarity and Effective Convergence and Extension Movements. *Current Biology*. 12:876-884.
- Matejcic, M., G. Salbreux, and C. Norden. 2018. A non-cell-autonomous actin redistribution enables isotropic retinal growth. *PLoS biology*. 16:e2006018.
- Mayer, M., M. Depken, J.S. Bois, F. Julicher, and S.W. Grill. 2010. Anisotropies in cortical tension reveal the physical basis of polarizing cortical flows. *Nature*. 467:617-621.
- Meyer, Emily J., A. Ikmi, and Matthew C. Gibson. 2011. Interkinetic Nuclear Migration Is a Broadly Conserved Feature of Cell Division in Pseudostratified Epithelia. *Current Biology*. 21:485-491.
- Munro, E., J. Nance, and J.R. Priess. 2004. Cortical flows powered by asymmetrical contraction transport PAR proteins to establish and maintain anterior-posterior polarity in the early *C. elegans* embryo. *Developmental cell*. 7:413-424.
- Murrell, M.P., and M.L. Gardel. 2012. F-actin buckling coordinates contractility and severing in a biomimetic actomyosin cortex. *Proceedings of the National Academy of Sciences of the United States of America*. 109:20820-20825.
- Nicolas-Perez, M., F. Kuchling, J. Letelier, R. Polvillo, J. Wittbrodt, and J.R. Martinez-Morales. 2016. Analysis of cellular behavior and cytoskeletal dynamics reveal a constriction mechanism driving optic cup morphogenesis. *Elife*. 5.

- Norden, C. 2017. Pseudostratified epithelia - cell biology, diversity and roles in organ formation at a glance. *Journal of cell science*. 130:1859-1863.
- Norden, C., S. Young, B.A. Link, and W.A. Harris. 2009. Actomyosin Is the Main Driver of Interkinetic Nuclear Migration in the Retina. *Cell*. 138:1195-1208.
- Oates, A.C., and R.K. Ho. 2002. Hairy/E(spl)-related (Her) genes are central components of the segmentation oscillator and display redundancy with the Delta/Notch signaling pathway in the formation of anterior segmental boundaries in the zebrafish. *Development (Cambridge, England)*. 129:2929-2946.
- Petrie, R.J., H. Koo, and K.M. Yamada. 2014. Generation of compartmentalized pressure by a nuclear piston governs cell motility in a 3D matrix. *Science (New York, N.Y.)*. 345:1062-1065.
- Phng, L.-K., V. Gebala, K. Bentley, A. Philippides, A. Wacker, T. Mathivet, L. Sauter, F. Stanchi, H.-G. Belting, M. Affolter, and H. Gerhardt. 2015. Formin-Mediated Actin Polymerization at Endothelial Junctions Is Required for Vessel Lumen Formation and Stabilization. *Developmental cell*. 32:123-132.
- Reinsch, S., and P. Gonczy. 1998. Mechanisms of nuclear positioning. *Journal of cell science*. 111 (Pt 16):2283-2295.
- Reymann, A.C., J.L. Martiel, T. Cambier, L. Blanchoin, R. Boujemaa-Paterski, and M. They. 2010. Nucleation geometry governs ordered actin networks structures. *Nature materials*. 9:827-832.
- Roman, W., and E.R. Gomes. 2018. Nuclear positioning in skeletal muscle. *Seminars in cell & developmental biology*. 82:51-56.
- Rowat, A.C., D.E. Jaalouk, M. Zwerger, W.L. Ung, I.A. Eydelnant, D.E. Olins, A.L. Olins, H. Herrmann, D.A. Weitz, and J. Lammerding. 2013. Nuclear envelope composition determines the ability of neutrophil-type cells to passage through micron-scale constrictions. *The Journal of biological chemistry*. 288:8610-8618.
- Sauer, F.C. 1935. Mitosis in the neural tube. *Journal of Comparative Neurology*. 62:377-405.
- Schindelin, J., I. Arganda-Carreras, E. Frise, V. Kaynig, M. Longair, T. Pietzsch, S. Preibisch, C. Rueden, S. Saalfeld, B. Schmid, J.Y. Tinevez, D.J. White, V. Hartenstein, K. Eliceiri, P. Tomancak, and A. Cardona. 2012. Fiji: an open-source platform for biological-image analysis. *Nature methods*. 9:676-682.
- Shu, T., R. Ayala, M.D. Nguyen, Z. Xie, J.G. Gleeson, and L.H. Tsai. 2004. Ndel1 operates in a common pathway with LIS1 and cytoplasmic dynein to regulate cortical neuronal positioning. *Neuron*. 44:263-277.
- Sidhaye, J., and C. Norden. 2017. Concerted action of neuroepithelial basal shrinkage and active epithelial migration ensures efficient optic cup morphogenesis. *Elife*. 6.
- Soo, F.S., and J.A. Theriot. 2005. Large-scale quantitative analysis of sources of variation in the actin polymerization-based movement of *Listeria monocytogenes*. *Biophysical journal*. 89:703-723.
- Steigemann, P., C. Wurzenberger, M.H. Schmitz, M. Held, J. Guizetti, S. Maar, and D.W. Gerlich. 2009. Aurora B-mediated abscission checkpoint protects against tetraploidization. *Cell*. 136:473-484.
- Strzyz, P.J., H.O. Lee, J. Sidhaye, I.P. Weber, L.C. Leung, and C. Norden. 2015. Interkinetic nuclear migration is centrosome independent and ensures apical cell division to maintain tissue integrity. *Developmental cell*. 32:203-219.
- Strzyz, P.J., M. Matejczic, and C. Norden. 2016. Heterogeneity, Cell Biology and Tissue Mechanics of Pseudostratified Epithelia: Coordination of Cell Divisions and

- Growth in Tightly Packed Tissues. *International review of cell and molecular biology*. 325:89-118.
- Swift, J., I.L. Ivanovska, A. Buxboim, T. Harada, P.C. Dingal, J. Pinter, J.D. Pajerowski, K.R. Spinler, J.W. Shin, M. Tewari, F. Rehfeldt, D.W. Speicher, and D.E. Discher. 2013. Nuclear lamin-A scales with tissue stiffness and enhances matrix-directed differentiation. *Science (New York, N.Y.)*. 341:1240104.
- Thisse, C., B. Thisse, T.F. Schilling, and J.H. Postlethwait. 1993. Structure of the zebrafish *snail1* gene and its expression in wild-type, spadetail and no tail mutant embryos. *Development (Cambridge, England)*. 119:1203-1215.
- Thoresen, T., M. Lenz, and M.L. Gardel. 2011. Reconstitution of contractile actomyosin bundles. *Biophysical journal*. 100:2698-2705.
- Thoresen, T., M. Lenz, and M.L. Gardel. 2013. Thick filament length and isoform composition determine self-organized contractile units in actomyosin bundles. *Biophysical journal*. 104:655-665.
- Totsukawa, G., Y. Yamakita, S. Yamashiro, D.J. Hartshorne, Y. Sasaki, and F. Matsumura. 2000. Distinct roles of ROCK (Rho-kinase) and MLCK in spatial regulation of MLC phosphorylation for assembly of stress fibers and focal adhesions in 3T3 fibroblasts. *The Journal of cell biology*. 150:797-806.
- Tran, P.T., L. Marsh, V. Doye, S. Inoue, and F. Chang. 2001. A mechanism for nuclear positioning in fission yeast based on microtubule pushing. *The Journal of cell biology*. 153:397-411.
- Tsai, J.W., K.H. Bremner, and R.B. Vallee. 2007. Dual subcellular roles for LIS1 and dynein in radial neuronal migration in live brain tissue. *Nature neuroscience*. 10:970-979.
- Tsai, J.W., W.N. Lian, S. Kemal, A.R. Kriegstein, and R.B. Vallee. 2010. Kinesin 3 and cytoplasmic dynein mediate interkinetic nuclear migration in neural stem cells. *Nature neuroscience*. 13:1463-1471.
- Tsai, L.H., and J.G. Gleeson. 2005. Nucleokinesis in neuronal migration. *Neuron*. 46:383-388.
- Villefranc, J.A., J. Amigo, and N.D. Lawson. 2007. Gateway compatible vectors for analysis of gene function in the zebrafish. *Developmental dynamics : an official publication of the American Association of Anatomists*. 236:3077-3087.
- Wolf, K., M. Te Lindert, M. Krause, S. Alexander, J. Te Riet, A.L. Willis, R.M. Hoffman, C.G. Figdor, S.J. Weiss, and P. Friedl. 2013. Physical limits of cell migration: control by ECM space and nuclear deformation and tuning by proteolysis and traction force. *The Journal of cell biology*. 201:1069-1084.
- Wu, J., I.A. Kent, N. Shekhar, T.J. Chancellor, A. Mendonca, R.B. Dickinson, and T.P. Lele. 2014. Actomyosin pulls to advance the nucleus in a migrating tissue cell. *Biophysical journal*. 106:7-15.
- Yi, K., B. Rubinstein, J.R. Unruh, F. Guo, B.D. Slaughter, and R. Li. 2013. Sequential actin-based pushing forces drive meiosis I chromosome migration and symmetry breaking in oocytes. *The Journal of cell biology*. 200:567-576.

Tables

Parameter	Hindbrain	Retina
Starting positions (μm)	8.4 ± 1.1	6.7 ± 0.5
Variance of starting positions (μm^2)	15.01	4.16
Duration of apical migration (min)	13 ± 1	22 ± 2
Mean instantaneous velocity ($\mu\text{m}/\text{min}$)	0.63 ± 0.06	0.32 ± 0.04
Directionality ratio	0.63 ± 0.06	0.36 ± 0.07
Kurtosis of instantaneous velocity distribution	0.32	5.44
Normalized nuclear aspect ratio	0.01 ± 0.01	0.17 ± 0.01

Table 1. Nuclear migration kinetics and shape change parameters that differ between hindbrain and retina. Values shown represent mean \pm SEM. Starting positions: $p=0.0243$, F test; duration of apical migration: $p=0.0052$, Mann-Whitney test; instantaneous velocity: $p<0.0001$, Mann-Whitney test; normalized nuclear aspect ratio: $p<0.0001$, Mann-Whitney test.

Parameter	Straight tissues		Curved tissues	
	Hindbrain	MHBS	Retina	MHBC
Cell length (μm)	45.32 ± 1.16	38.27 ± 1.63	46.13 ± 1.32	41.54 ± 1.88
Apical-to-basal footprint ratio	1.25 ± 0.06	1.46 ± 0.12	2.32 ± 0.11	2.32 ± 0.17
Actin-nuclear signal crossover point (%)	9	11	29	20
Duration of apical migration (min)	13 ± 1	19 ± 2	22 ± 2	28 ± 2
Mean instantaneous velocity ($\mu\text{m}/\text{min}$)	0.63 ± 0.06	0.66 ± 0.08	0.32 ± 0.04	0.36 ± 0.04
Directionality ratio	0.63 ± 0.06	0.67 ± 0.01	0.36 ± 0.07	0.53 ± 0.01
Normalized nuclear aspect ratio	0.01 ± 0.01	0.12 ± 0.02	0.17 ± 0.01	0.24 ± 0.03

Table 2. Tissue architecture, nuclear migration kinetics, and shape change parameters that differ between straight and curved neuroepithelial tissues. Values shown represent mean \pm SEM. Cell length: $p_{(HB-MHBS)}=0.1017$, $p_{(R-MHBC)}=0.0053$, $p_{(HB-R)}=0.5780$, $p_{(MHBS-MHBC)}=0.0872$; apical-to-basal footprint ratio: $p_{(HB-MHBS)}=0.1312$, $p_{(R-MHBC)}=0.2617$, $p_{(HB-R)}<0.0001$, $p_{(MHBS-MHBC)}<0.0001$; duration of nuclear migration: $p_{(HB-MHBS)}=0.3540$, $p_{(R-MHBC)}=0.2457$, $p_{(HB-R)}=0.0052$, $p_{(MHBS-MHBC)}=0.0326$; instantaneous velocity: $p_{(HB-MHBS)}=0.9423$, $p_{(R-MHBC)}=0.7831$, $p_{(HB-R)}<0.0001$, $p_{(MHBS-MHBC)}=0.0038$; normalized nuclear aspect ratio: $p_{(HB-MHBS)}<0.0001$, $p_{(R-MHBC)}=0.0324$, $p_{(HB-R)}<0.0001$, $p_{(MHBS-MHBC)}=0.0221$, all p values calculated using Mann-Whitney test.

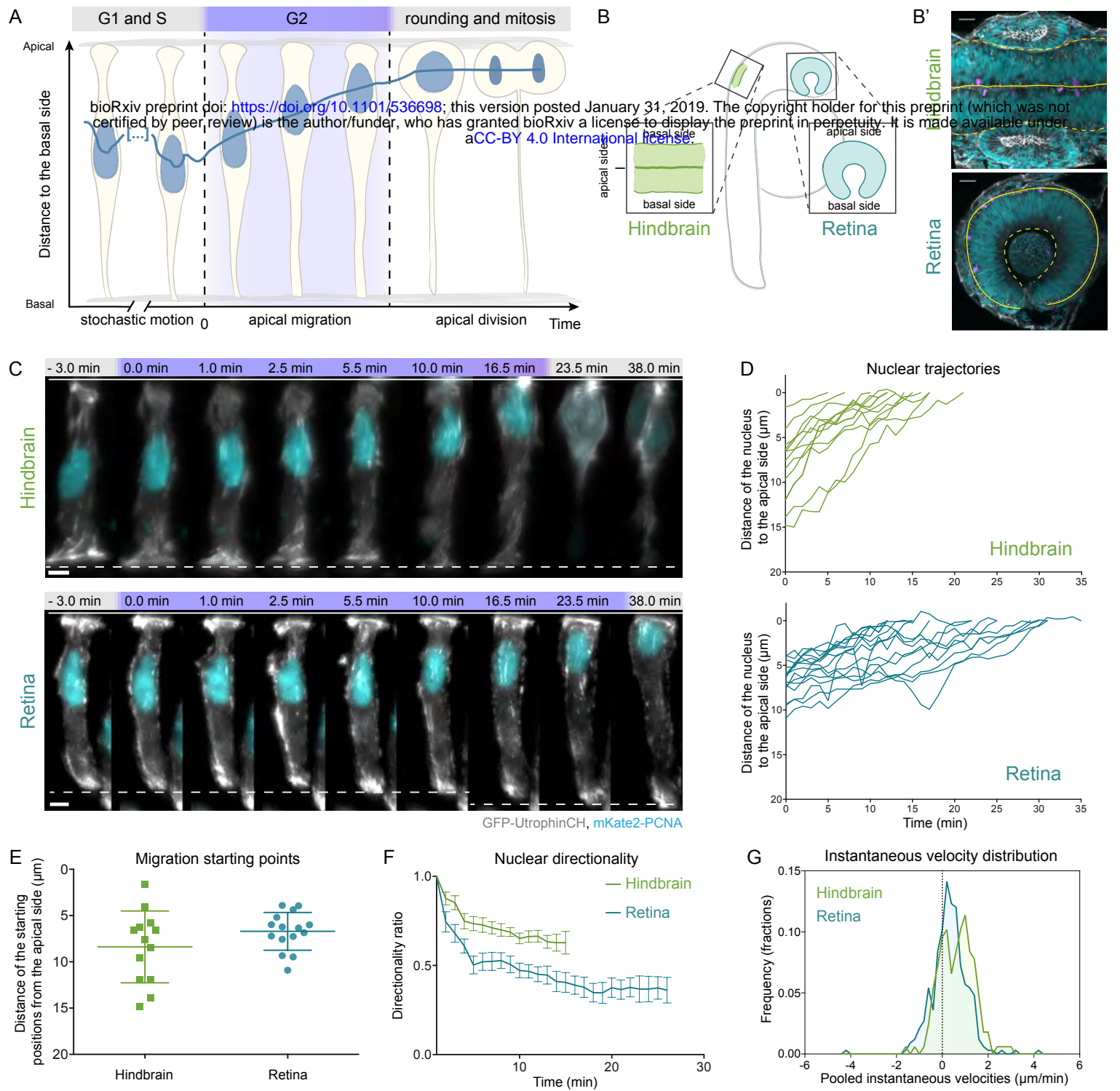


Figure 1. Apical nuclear migration in the hindbrain is faster and more directed than in the retina. (A) Neuroepithelial nuclei move stochastically in G1 and S and occupy diverse apico-basal positions. In G2 (highlighted in purple in the schematic and all montages), nuclei migrate to the apical side where cells round and divide. (B) Schematic of hindbrain and retinal neuroepithelia in the zebrafish embryo. Hindbrain is shown in green and retina in blue in all figures. (B') Morphology of hindbrain at 18 hpf and retina at 24 hpf. Nuclear staining: DAPI (cyan), actin staining: phalloidin (gray), mitotic cells: pH3 (magenta). Solid lines mark the apical and dashed lines mark the basal tissue surface in all figures. (C) Example of apical nuclear migration in maximum projection of hindbrain and retinal cells, imaged with LSFM (Video 1). mKate2-PCNA labels nuclei (cyan), GFP-UtrophinCH labels actin (gray). (D) Apical migration trajectories. Start: 0 min = entry in G2. Finish: onset of cell rounding (nuclear position at cell rounding = 0 μm from the apical side). (E) Starting positions of hindbrain and retinal nuclei shown as mean ± SD. $p=0.0243$, F-test. (F) Directionality ratios shown as mean of all tracks, error bars represent SEMs. Hindbrain = 0.63 ± 0.06 , Retina = 0.36 ± 0.07 . (G) Pooled instantaneous velocity distributions in hindbrain and retina. $p<0.0001$, Mann-Whitney test. Scale bars: (B') 20 μm, (C) 5 μm.

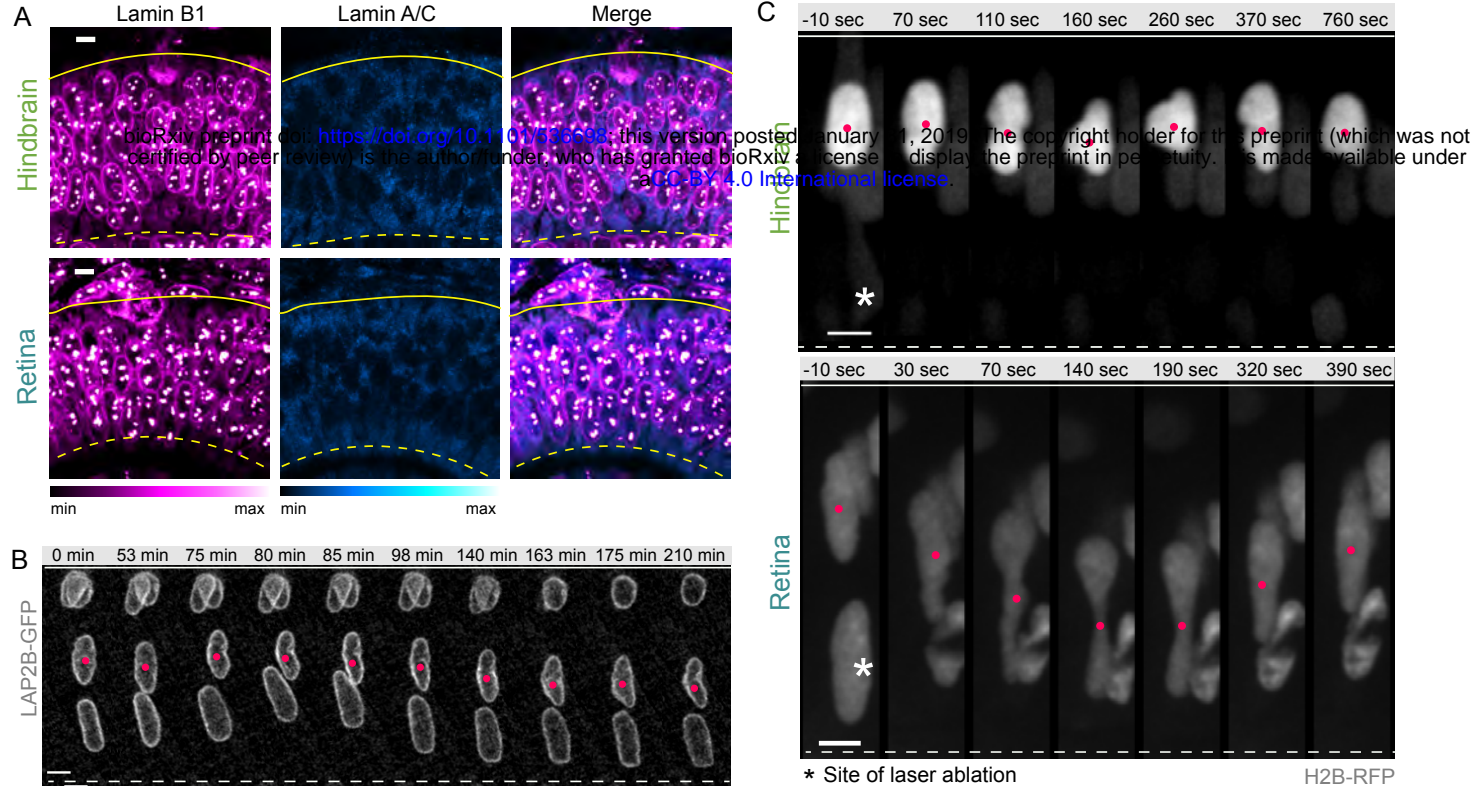


Figure 2. Hindbrain and retinal nuclei are deformable and experience different forces during apical nuclear migration.

(A) Immunostaining of Lamin B1, and Lamin A/C in hindbrain and retinal cells (lookup tables indicate minimal and maximal signal values). (B) Dynamics of nuclear deformations, visualized with nuclear envelope marker LAP2B-GFP. (C) Nuclear deformations upon perturbation with neuroepithelial integrity in hindbrain and retina using laser ablation (Video 2). Site of ablation is marked with an asterisk. (D) Examples of overexpression of Lamin A/C (LmnA-mKate2) in retinal neuroepithelium. LmnA-mKate2 localizes to the nuclear envelope and upon stronger overexpression additionally forms foci in the nucleoplasm. (E) Representative time-series of LmnA-mKate2 overexpressing cell (gray, upper

panel) unable to reach apical side, undergoing basal mitosis (Video 3). PCNA-GFP (green, lower panel) is used as a cell cycle marker. (F) 3D segmentation of hindbrain and retinal nuclei in S and G2. (G) Aspect ratio change between S and G2 for retinal and hindbrain nuclei. $p < 0.0001$, Mann-Whitney test. (H) Cross-correlation analysis of nuclear instantaneous velocity and aspect ratio changes in the retina shows increased correlation in G2. $p = 0.0024$, Wilcoxon signed-rank test. Scale bars: 5 μm .

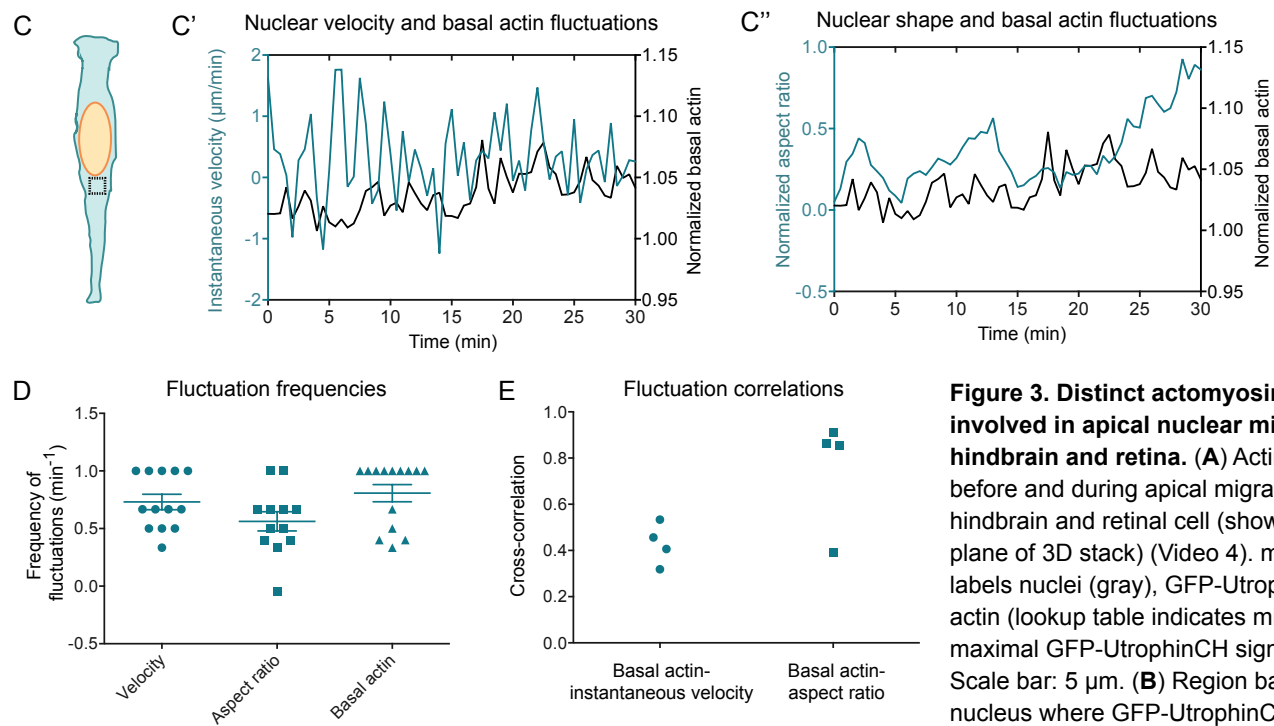
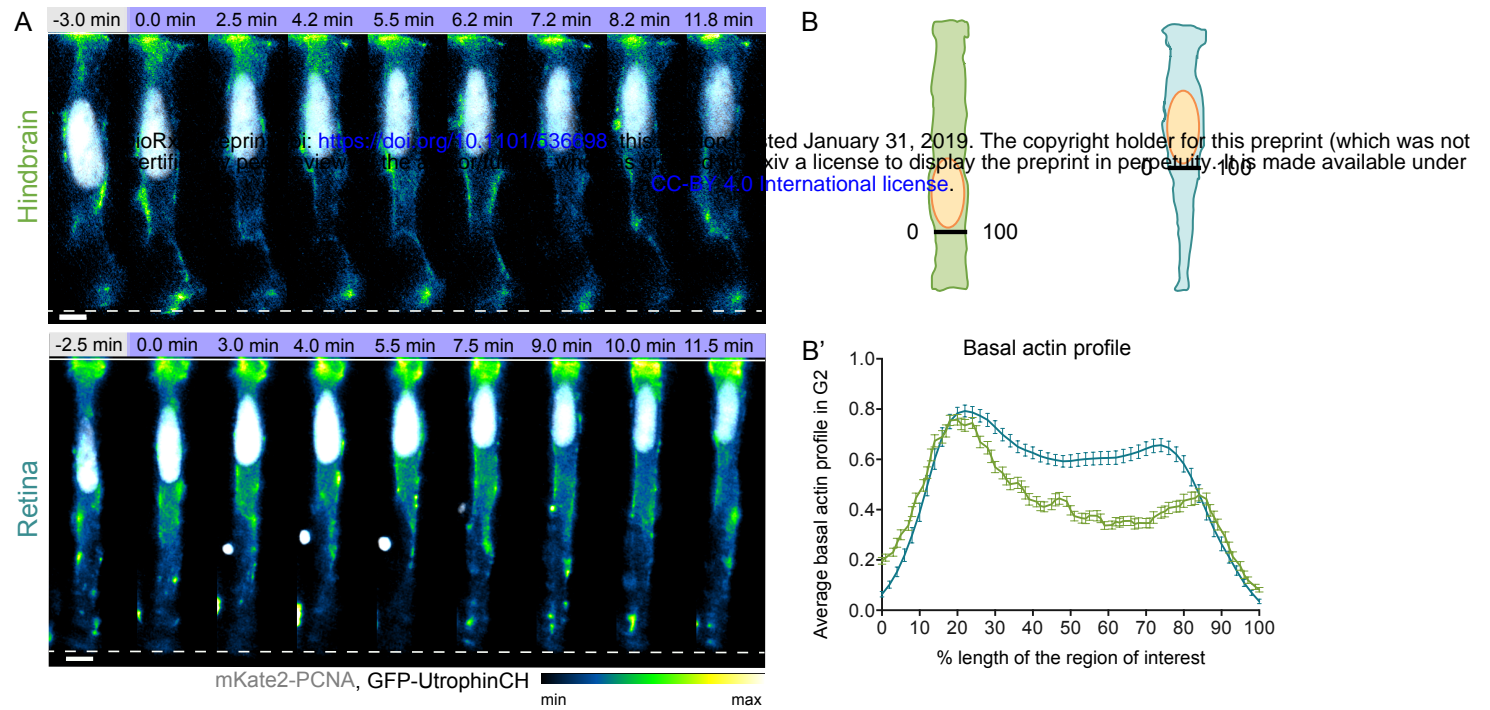


Figure 3. Distinct actomyosin pools are involved in apical nuclear migration in hindbrain and retina. (A) Actin distribution before and during apical migration in hindbrain and retinal cell (shown the central z plane of 3D stack) (Video 4). mKate2-PCNA labels nuclei (gray), GFP-UtrophinCH labels actin (lookup table indicates minimal and maximal GFP-UtrophinCH signal values). Scale bar: 5 μm . (B) Region basally of nucleus where GFP-UtrophinCH signal

intensity was measured in the cells shown in (A). (B') Normalized average intensity distribution of GFP-UtrophinCH signal. Shown mean profile of all G2 time points, error bars: SEM. (C) Region where average GFP-UtrophinCH fluorescence intensity was measured basally to nucleus in a SUM projection. (C', C'') Fluctuations in normalized basal actin plotted together with fluctuations in instantaneous velocity (C') and normalized nuclear aspect ratio (C'') in same retinal cell. (D) Pooled fluctuation frequencies of instantaneous velocity, nuclear aspect ratio, and basal actin intensity for the same retinal cell. Error bars: SEM. ($p=0.46$ and $p=0.05$ for velocity and aspect ratio respectively, Mann-Whitney test). (E) Cross-correlation analysis shows positive correlation between the fluctuations in basal actin and instantaneous velocity, as well as basal actin and nuclear aspect ratio.

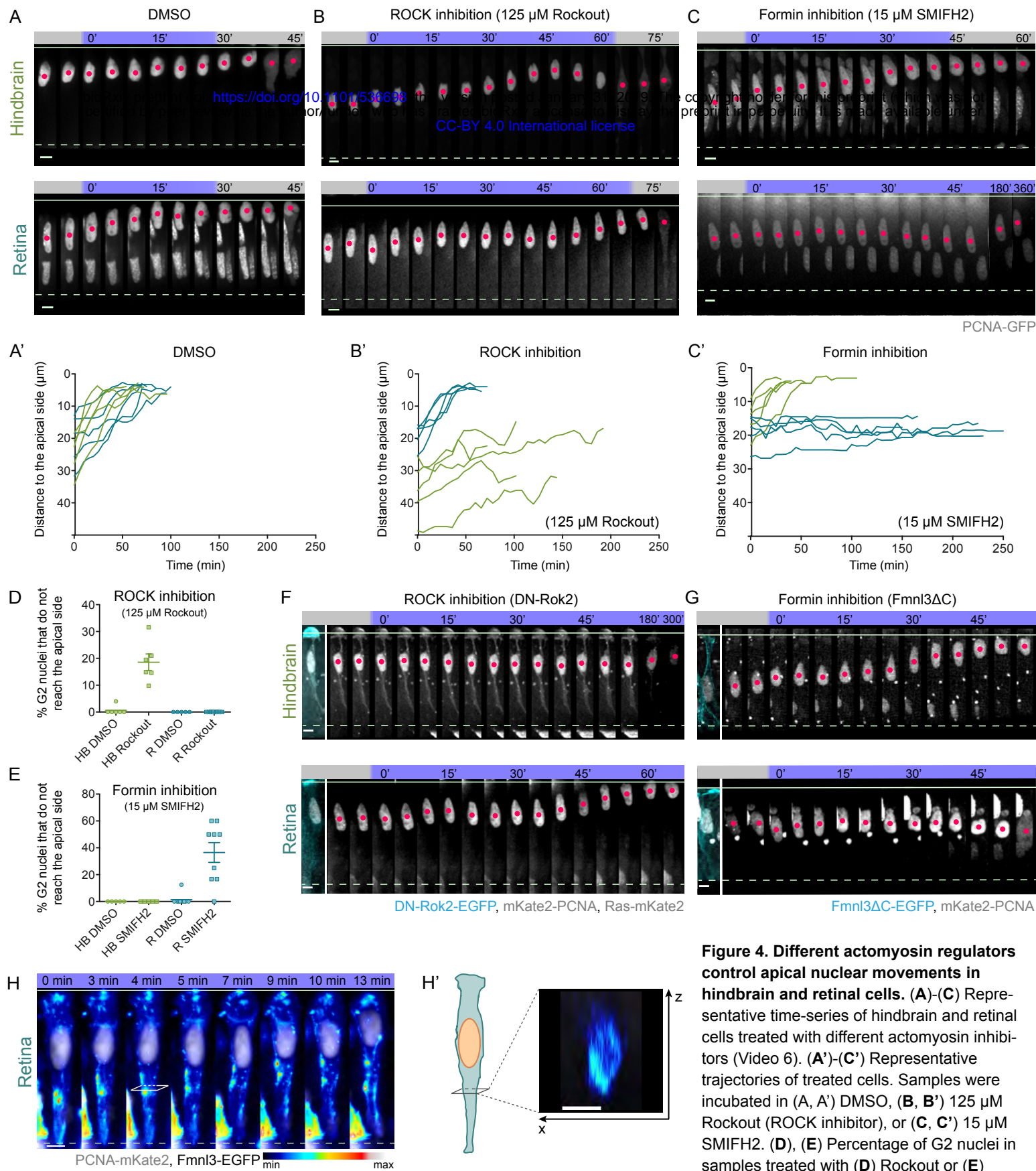


Figure 4. Different actomyosin regulators control apical nuclear movements in hindbrain and retinal cells. (A)-(C) Representative time-series of hindbrain and retinal cells treated with different actomyosin inhibitors (Video 6). (A')-(C') Representative trajectories of treated cells. Samples were incubated in (A, A') DMSO, (B, B') 125 μ M Rockout (ROCK inhibitor), or (C, C') 15 μ M SMIFH2. (D), (E) Percentage of G2 nuclei in samples treated with (D) Rockout or (E) SMIFH2 unable to reach the apical side in hindbrain and retina. Error bars: SEM. ($p=0.0001$ for Rockout-treated and $p=0.0050$ for SMIFH2-treated samples, Mann-Whitney test) (F), (G) Representative time-series of hindbrain and retinal cells expressing heat shock induced (F) DN-Rok2-EGFP (cyan), PCNA-GFP (gray) or (G) Fmnl3 Δ C-EGFP (cyan), mKate2-PCNA (gray) (Video 8). (H) Representative cell showing the distribution of Fmnl3-EGFP (maximum intensity projection, lookup table indicates minimal and maximal Fmnl3-EGFP signal values) in retinal cell (Video 9). (H') Orthogonal (x-z) cross-section of the basal cell process of retinal cells. Fmnl3-EGFP is seen enriched basally of the nucleus. Scale bars: 5 μ m.

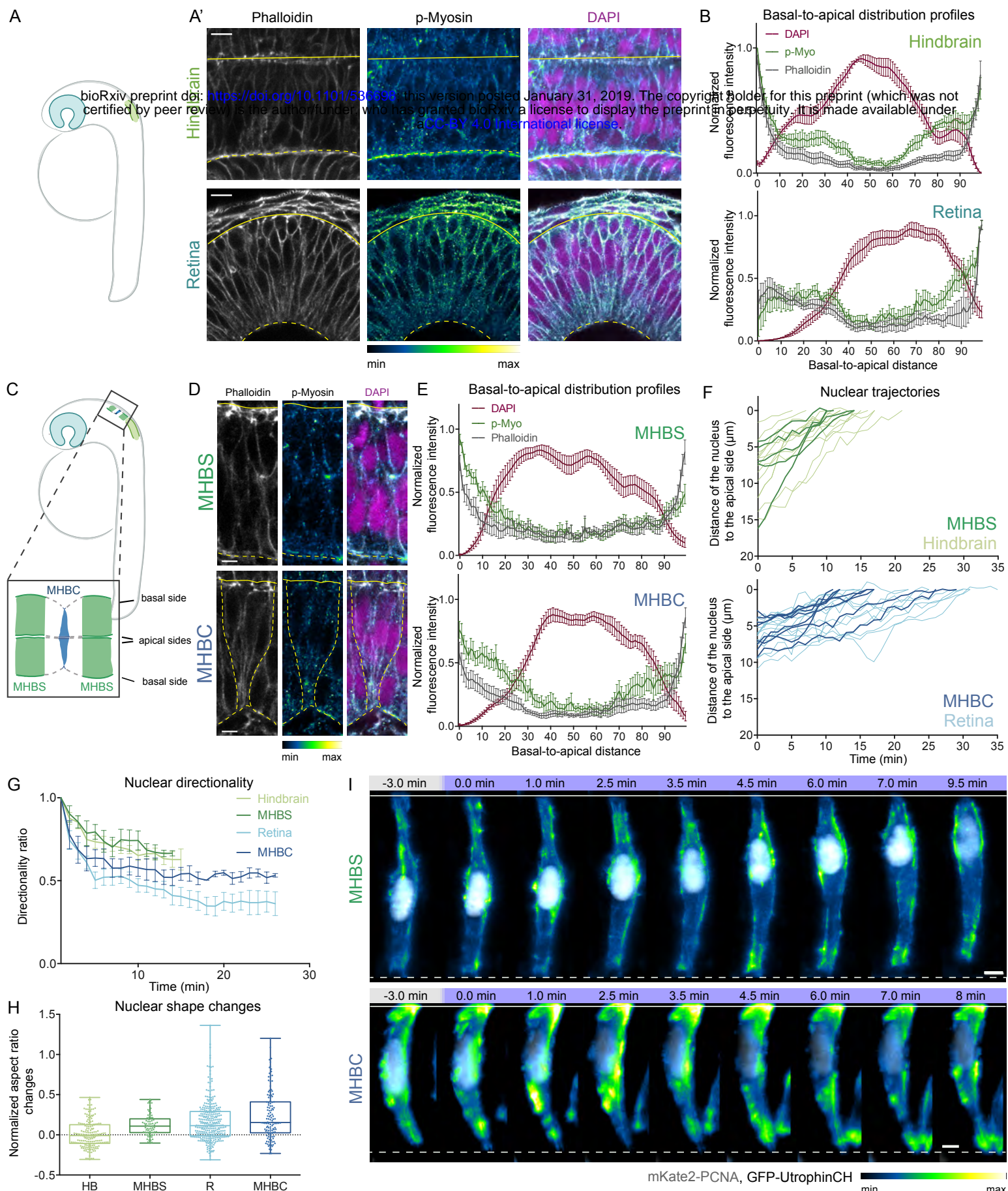
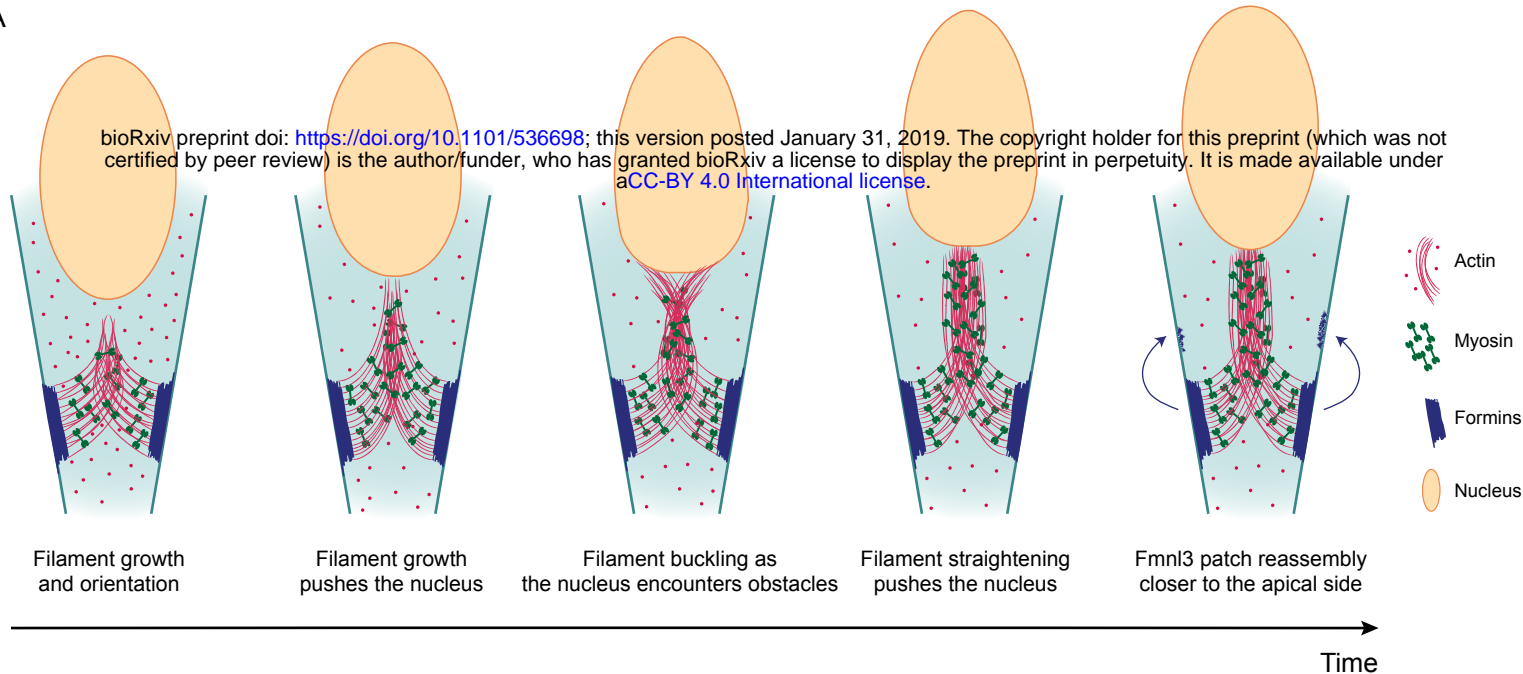


Figure 5. Different actin-dependent mechanisms of apical nuclear migration are linked to cell and tissue shape. (A) Schematic of the position and morphology of hindbrain and retinal neuroepithelia. (A') Distribution of phalloidin (actin, gray), p-Myo (active (phosphorylated) myosin, lookup table indicates minimal and maximal signal values), and DAPI (nuclei, magenta) in hindbrain and retinal neuroepithelia. (B) Normalized average intensity distributions of phalloidin, p-Myo, and DAPI along the apicobasal axis of hindbrain and retinal neuroepithelium. The mean of all samples is shown, error bars: SEM. (C) Schematic of the position and morphology of MHBS and MHBC neuroepithelia. MHBS: dark green, MHBC: dark blue. (D) Distribution of phalloidin (actin, gray), p-Myo (active (phosphorylated) myosin, lookup table indicates minimal and maximal signal values), and DAPI (nuclei, magenta) in MHBS and MHBC neuroepithelia. (E) Normalized average intensity distributions of phalloidin, p-Myo, and DAPI signal in MHBC and MHBS. The mean of all samples is shown, error bars: SEM. (F) MHBS and MHBC nuclear trajectories compared to hindbrain and retinal trajectories. Hindbrain and retinal trajectories correspond to Fig. 1d. (G) Directionality ratios of MHBS and MHBC nuclei. The mean of all tracks is shown with hindbrain and retinal data corresponding to Figure 1f. Error bars: SEM. Final directionality ratios: MHBS = 0.67 ± 0.01 , MHBC = 0.53 ± 0.01 . (H) Nuclear aspect ratio changes between S and G2 in MHBC and MHBS

($p=0.0221$, Mann-Whitney test). Boxes extend from 25th to 75th percentiles, whiskers extend from smallest to largest value. (I) Actin distribution before and during apical migration in MHBS and MHBC cell (shown maximum projection of 3D stack's central 5 z-planes) (Video 10). mKate2-PCNA labels nuclei (gray), GFP-UtrophinCH labels actin (lookup table indicates minimal and maximal GFP-UtrophinCH signal values). Aspect ratio changes in hindbrain and retina correspond to Fig. 2 G. Scale bars: (A) 10 μm , (D), (I) 5 μm .

bioRxiv preprint doi: <https://doi.org/10.1101/536698>; this version posted January 31, 2019. The copyright holder for this preprint (which was not certified by peer review) is the author/funder, who has granted bioRxiv a license to display the preprint in perpetuity. It is made available under aCC-BY 4.0 International license.

A



B

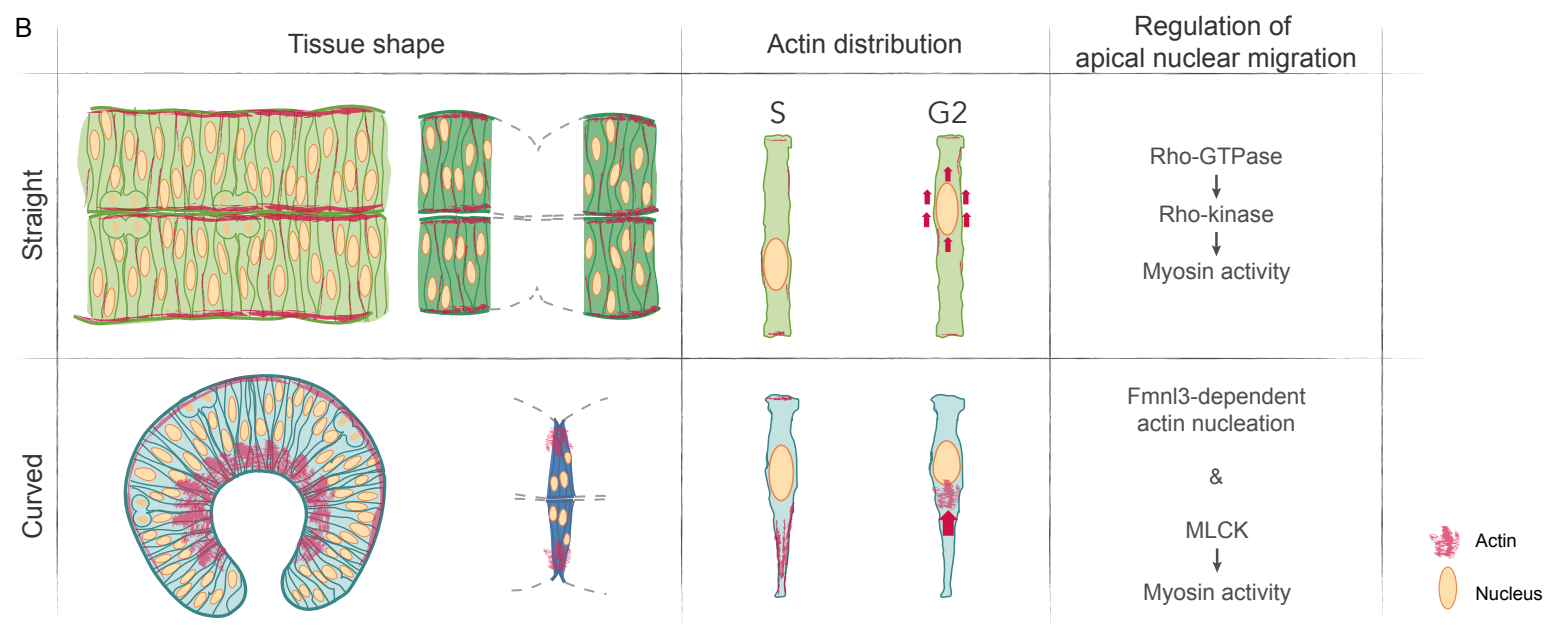


Figure 6. Distinct actomyosin distribution in straight and curved tissues can be a prerequisite for different force generation in apical nuclear migration.

(A) Schematic representation of proof-of-principle mathematical model explaining the pushing mechanism of apical nuclear migration in the retina. For details of theoretical model see Supplemental Material. (B) Schematic summary of suggested links between tissue shape and mechanisms of apical nuclear migration. Straight and curved tissues show different distributions of actomyosin. In straight tissues actomyosin is evenly distributed along the lateral sides of cells. An enrichment of actomyosin is observed baso-laterally in curved tissues. A basal actomyosin network that pushes the nucleus to the apical side could thus only be formed in cells of curved, but not straight tissues.

Supplemental material to

Tissue shape determines actin-dependent nuclear migration mechanisms in neuroepithelia

Iskra Yanakieva, Anna Erzberger, Marija Matejčić, Carl D. Modes and Caren Norden

Proof-of-Principle Model of a Nuclear Migration Mechanism in Retinal Neuroepithelia

1 Critical Buckling & Saltatory Dynamics

We first need to calculate the critical buckling length for an f-actin filament or bundle. We use as many measured or approximate community-accepted values as possible and can “fit” or extract information about those that remain free from the observed dynamics. We also here assume that the timescale for any viscoelastic relaxation of the f-actin bundles is slower than the relevant buckling dynamics. For classical Euler buckling, the critical buckling length is given by [1]:

$$L_c = c_{bc}\pi \left(\frac{\kappa_B}{F} \right)^{1/2} \quad (1)$$

for $c_{bc} = 1/2$ in the case of one clamped and one free end of the filament. κ_B is the bending stiffness of the filament or bundle and F is the applied compressional force. For the applied force, we are deep into the regime of low Reynolds number and may assume a Stokes’ drag scenario for the nucleus being pushed through the cytoplasm by the f-actin. This gives the following equation for F :

$$F = 6\pi\eta Rv \quad (2)$$

for η the effective dynamic viscosity of cytoplasm at the length scale of the nucleus, R the radius of the nucleus, and v the flow velocity. Meanwhile, for bundled f-actin filaments the bending stiffness is given by [2]:

$$\kappa_B = \kappa_f N \left[1 + \frac{A_f(N-1)(d_f+t)^2/12I_f}{1+c(q_j)\frac{N+\sqrt{N}}{\alpha}} \right]. \quad (3)$$

Here κ_f is the bending stiffness of a single strand of f-actin, N is the number of filaments in the bundle, and A_f, d_f, t , and I_f are geometric properties of the actin monomers and the cross-linker spacings. $c(q_j) \approx 1$ for the low relevant mode numbers with our boundary conditions. α is a unitless parameter that measures the relative importance of the cross-linker shear stiffness, $\alpha = 0$ in the limit of low shear stiffness and $\alpha \rightarrow \infty$ for very high shear stiffness. If we assume that myosin is coordinating and cross-linking the bundles, then α is likely to be very low and we may approximate $\kappa_B \approx \kappa_f N$.

To show a proof-of-principle for the hypothesis that the buckling is relevant for the migration mechanics, we would expect a plausible set of these parameters in the above equations to allow for an L_c of order $1-10\mu m$, which would match the experimentally observed distances between the anchoring formin domain

and the basal side of the nucleus. The following values were approximated for the needed parameters:

$$\begin{aligned}\eta &\approx 5 * 10^{-2} Pa \text{ sec} \\ R &\approx 3 * 10^{-6} m \\ v &\approx 1.6 * 10^{-8} m/sec \\ \kappa_f &\approx 10^{-25} Nm^2\end{aligned}$$

with η and κ taken from the literature [3, 4] and R and v taken from our own observations.

Under these approximations we indeed find that L_c is plausibly in the neighborhood of $1 - 10\mu m$, consistent with the observations regarding the trailing formin attachments. N can easily be taken to be up to 20 or so without pushing L_c out of a plausible range. Furthermore, increasing the shear stiffness of the cross-linkers in any putative bundling would only serve to push the overall bending stiffness of the bundle out of range on the top end, providing some circumstantial evidence that the shear-soft myosins serve as the primary cross-linkers.

The sensitivity of L_c to the effective dynamic viscosity allows our proof-of-principle model to qualitatively explain the saltatory motion of the nucleus as well. In the crowded environment of the PSE, the effective η seen by the traveling nucleus can vary widely as intra-cellular machinery or compartments are encountered or stiffer, interposing regions from neighboring cells, associated, for example, with the locations of their nuclei crowd the local environment. All of these things can serve to temporarily increase the compressive force acting on the actin filaments and bundles, leading to lower critical buckling threshold lengths. As the filaments buckle, continued polymerization at the formin-anchored end no longer moves the nucleus forward but instead increases the curvature of the buckled filament, adding to the stored stress and hence the force delivered to the nucleus. Eventually, the rising stress in the buckled filaments provides enough force to push the nucleus past whatever local road block caused the buckling in the first place. When this occurs, the filaments can then rapidly straighten, causing a burst of increased velocity for the nucleus. It is likely that the force required to resolve these impediments is directly related to the deformability of the nuclear envelope, potentially explaining why Lamin A over expression slowed migration, as greater forces on the nucleus and stresses in the filaments would be required, increasing the frequency with which individual filaments might undergo critical failure and subsequent depolymerization.

This picture of f-actin growth pushing the nucleus forward with alternating periods in which the polymerization leads directly to increased displacement of the nucleus and in which it leads instead to rising forces delivered to a stalled nucleus does make one key prediction. Because the motion of the nucleus is driven directly by the polymerization, and the displacement after stalls are resolved is again simply the length of the actin bundle, then the average speed of the nucleus over its migratory period should very closely match the speed of f-actin polymerization. And indeed, formin-catalyzed f-actin polymerization is known to be approximately [5]:

$$k_+ \approx 0.3 \mu m/min.$$

which is very much in line with our observations of the average velocity of the migrating nucleus.

References

- [1] J. Kierfeld, P. Gutjahr, *et al.* “Buckling, Bundling, and Pattern Formation: From Semi-Flexible Polymers to Assemblies of Interacting Filaments.” *J. Comput. Theor. Nanosci.* **6**(3) 1-14 (2006).
- [2] M. Bathe, C. Heussinger, *et al.* “Cytoskeletal Bundle Mechanics.” *Biophys. J.* **94** 2955-2964 (2008).
- [3] T. Kalwarczyk, N. Ziebac, *et al.* “Comparative Analysis of Viscosity of Complex Liquids and Cytoplasm of Mammalian Cells at the Nanoscale.” *Nano letters* **11** 2157-63 (2011).
- [4] F. Gittes, B. Mickey, *et al.* “Flexural rigidity of microtubules and actin filaments measured from thermal fluctuations in shape.” *J. Cell Biol.* **120**(4) 923-34 (1993).
- [5] P. Hotulainen and P. Lappalainen, “Stress fibers are generated by two distinct actin assembly mechanisms in motile cells.” *J. Cell Biol.* **173**(3) 383-394 (2006).

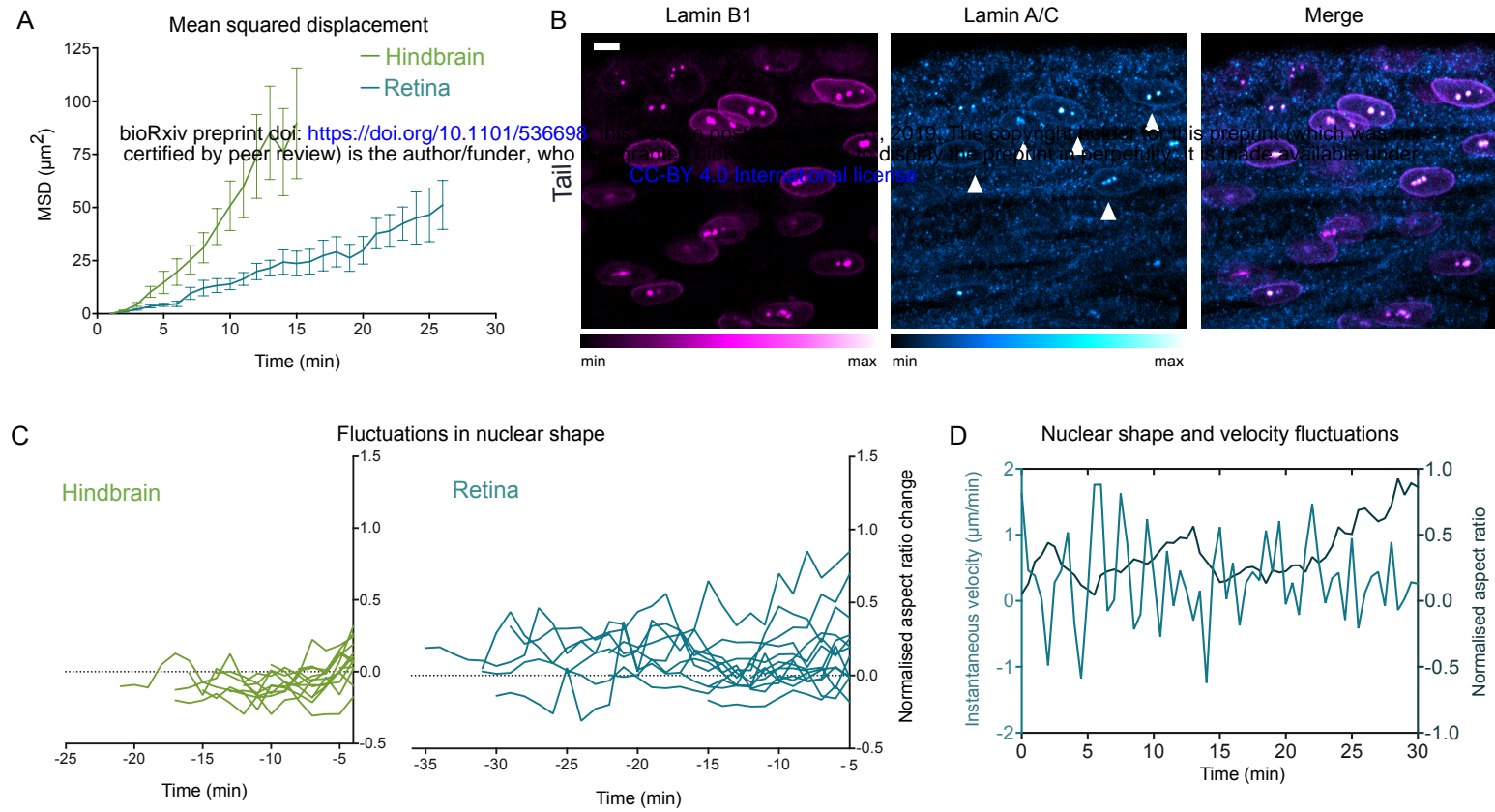


Figure S1. Hindbrain and retinal nuclei move and deform differently during apical nuclear migration. Related to Fig. 1 and 2. **(A)** Mean squared displacement of hindbrain and retinal cell apical migration. Mean of all tracks is shown, error bars: SEM. **(B)** Control staining of Lamin A/C in the tail of a 24 hpf zebrafish (lookup tables indicate minimal and maximal Lamin B1 and Lamin A/C signal values). Scale bar: 10 μm . **(C)** Normalized aspect ratio changes of individual hindbrain and retinal nuclei with time. **(D)** Fluctuations of mean instantaneous velocity and normalized nuclear aspect ratio with time in representative retinal cell.

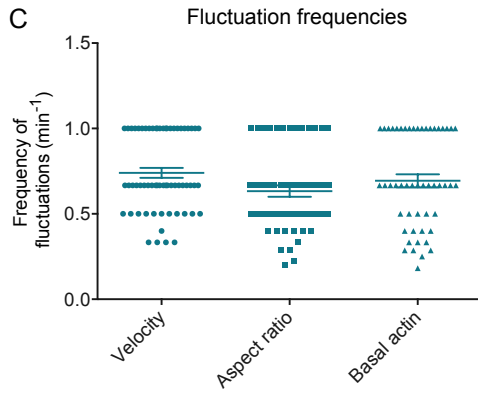
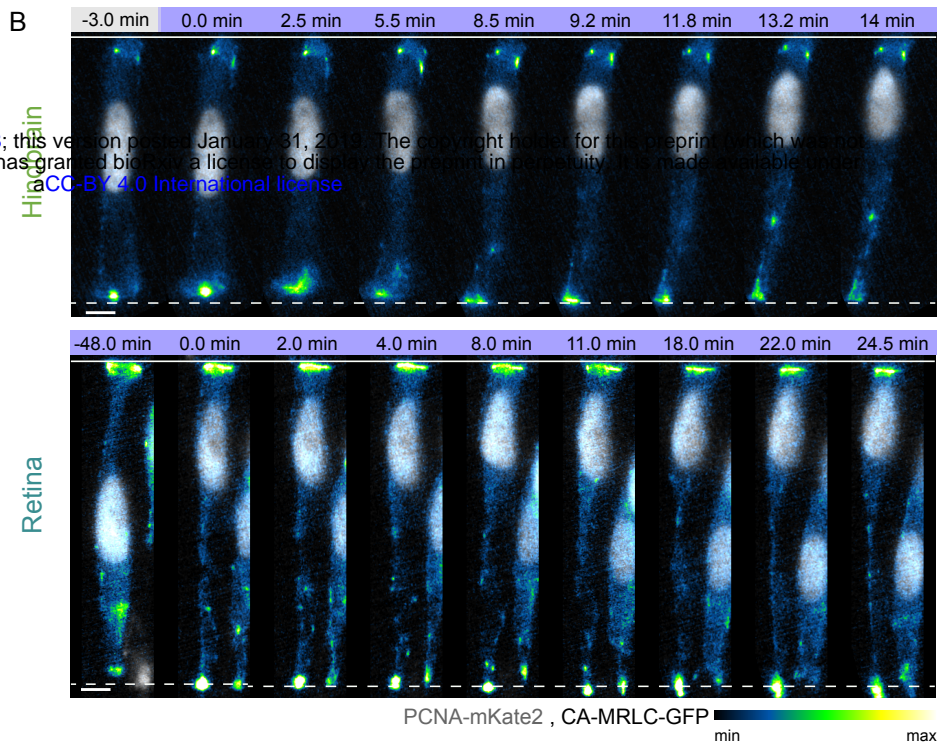
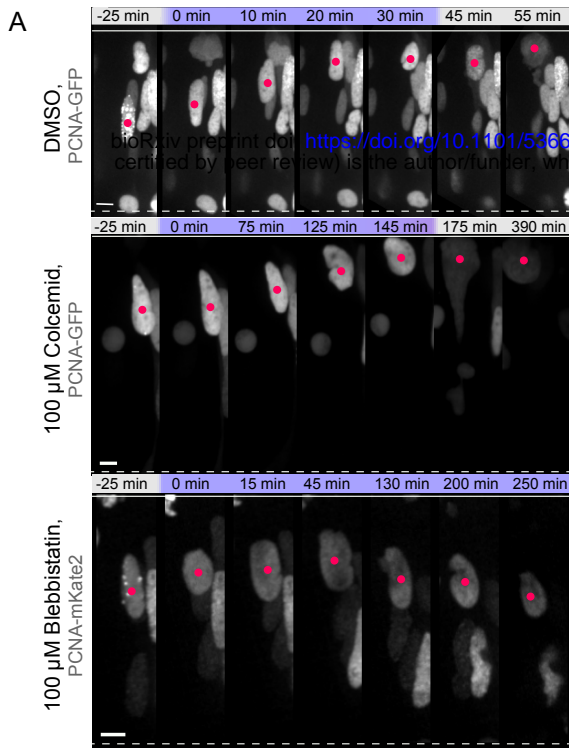
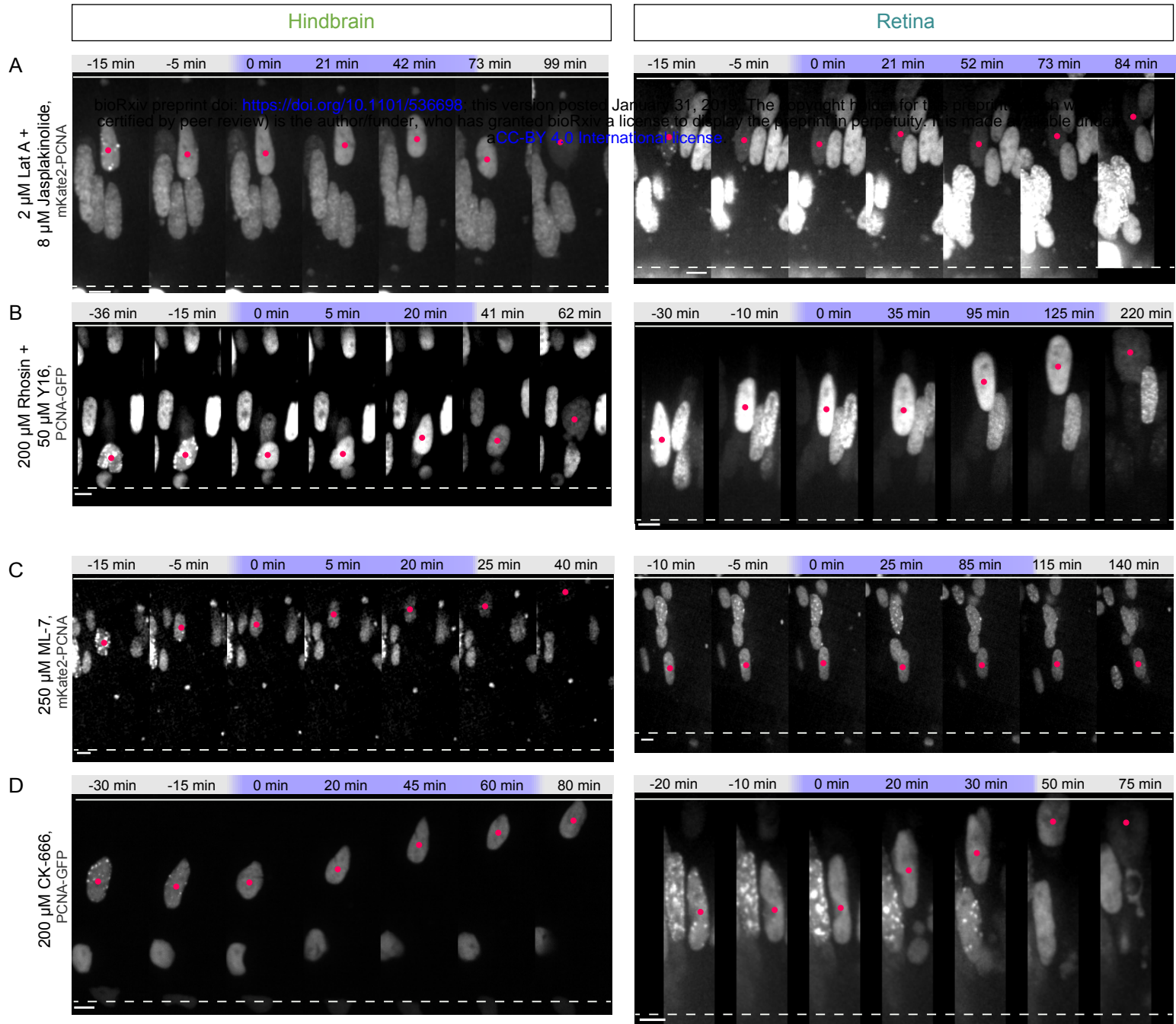


Figure S2. Apical nuclear migration in the hindbrain depends on actomyosin but myosin distribution differs in hindbrain and retinal cells. Related to Fig. 3. **(A)** Representative time-series of cells treated with different cytoskeletal inhibitors in hindbrain and retina (Video 5). Samples were incubated in DMSO, 100 μ M Colcemid (microtubule polymerization inhibitor), or 100 μ M Blebbistatin (myosin II inhibitor). **(B)** Myosin distribution upon apical migration in a single hindbrain (upper) and retinal (lower) cell. mKate2-PCNA labels nuclei (gray), CA-MRLC-GFP labels active myosin (lookup table indicates minimal and maximal CA-MRLC-GFP signal values). **(C)** Pooled frequencies of oscillation of instantaneous velocity, nuclear aspect ratio, and basal actin intensity for four retinal cells. Error bars: SEM. ($p=0.3372$ and $p=0.2399$ for velocity and aspect ratio respectively, Mann-Whitney test). Scale bars: 5 μ m.



E

Small molecule inhibitor	Inhibited process	Apical migration perturbed	
		Hindbrain	Retina
Colcemid	Microtubule polymerization	no	no
Blebbistatin	Myosin II activity	yes	yes
Jasplakinolide + Latrunculin A	Actin filament turnover	yes	yes
Rhosin + Y16	Rho-GTPase activity	yes	no
Rockout	Rho-kinase activity	yes	no
ML-7	MLCK activity	no	yes
CK-666	Arp2/3-dependent actin nucleation	no	no
SMIFH2	Formin-dependent actin nucleation	no	yes

Figure S3. Apical nuclear migration in hindbrain and retina is controlled by different actomyosin regulators. Related to Fig. 4. (A)-(D) Representative time-series of cells treated with different inhibitors of actomyosin dynamics in hindbrain and retina (Video 7). Samples were incubated in (A) 2 μ M Latrunculin A (actin polymerization inhibitor) and 8 μ M Jasplakinolide (microfilament turnover inhibitor), (B) 200 μ M Rhosin

and 50 μ M Y16 (RhoA-GTPase inhibitors), (C) 250 μ M ML-7 (MLCK inhibitor), or (D) 200 μ M CK-666 (Arp2/3 inhibitor). Scale bars: 5 μ m. (E) Table summarizing the effects of actomyosin dynamics perturbation experiments on apical nuclear migration in hindbrain and retina.

bioRxiv preprint doi: <https://doi.org/10.1101/536698>; this version posted January 31, 2019. The copyright holder for this preprint (which was not certified by peer review) is the author/funder, who has granted bioRxiv a license to display the preprint in perpetuity. It is made available under aCC-BY 4.0 International license.

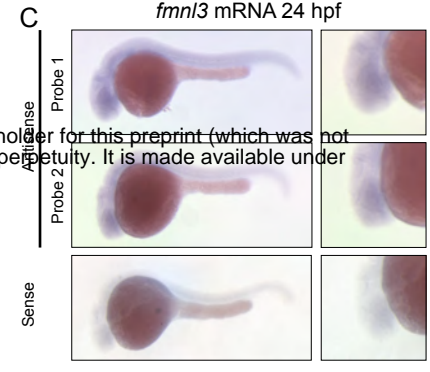
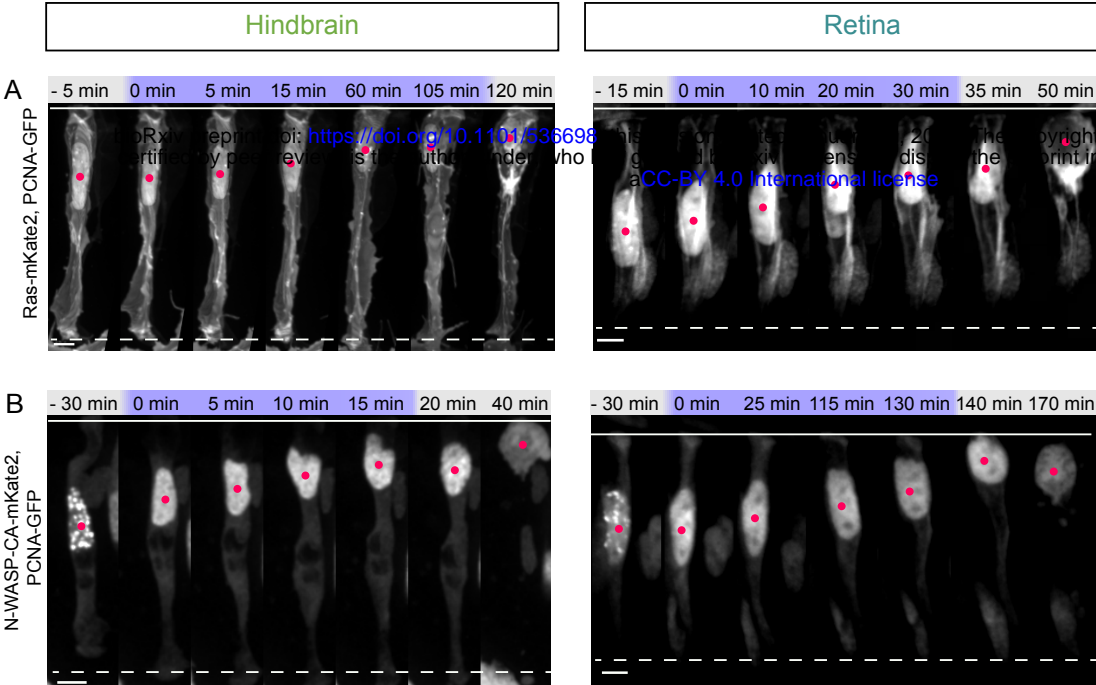


Figure S4. Actin polymerization factors involved in apical migration. Related to Fig. 4. (A), (B) Representative time-series of hindbrain and retinal cells expressing (A) control Ras-mKate2 and PCNA-GFP (both in gray) or (B) heat-shock induced dominant negative mKate2-N-WASP-CA and PCNA-GFP (both in gray) (Video 8). N-WASP inhibition did not perturb apical migration in hindbrain (C) In situ hybridization analysis demonstrates that *Fmn13* is expressed in the retina at 24 hpf. Scale bars: 5 μ m.

Supplementary tables

Construct	Labelled structure/ Function	Reference
hsp70: Ras-mKate2	Cell membrane	19
bactin: mKate2-Ras	Cell membrane	33
hsp70: GFP-UtrophinCH	F-actin	19
hsp70: PCNA-GFP	Cell cycle phase marker	33
hsp70: DN-Rok2-EGFP/ mKate	Dominant negative Rho-kinase	This study
hsp70: mKate2-N-WASP-CA	C-terminal domain of the Arp2/3 activator N-WASP	33
hsp70: EGFP-LAP2b	Lamina-associated polypeptide 2	This study
hsp70: LMNA-mKate2	Lamin A	This study
hsp70: Fmn13-EGFP	Fmn13	This study
hsp70: Fmn13 Δ C-EGFP	Truncated Fmn13	Recloned from ³⁴
pCS2+ Ras-mKate2	Cell membrane	63
pCS2+ Ras-GFP	Cell membrane	19
pCS2+ H2B-RFP	Chromatin	16
pCS2+ GFP-UtrophinCH	F-actin	64
pCS2+ Lifeact-GFP	F-actin	Kind gift from Oates lab
pCS2+ MRLC2 ^{T18DS19D} -GFP	Constitutively activated myosin light chain	19
pCS2+ PCNA-GFP	Cell cycle phase marker	(Leung, Klopper et al., 2011)
pCS2+ mKate2-PCNA	Cell cycle phase marker	This study

Supplementary Table 1. List of constructs.

Chemical	Inhibited process	Working concentration	Source/ Cat.No.
Blebbistatin	Myosin II activity	100 μ M	Enzo Life Sciences/ BML-EI315-0005
Colcemid	Microtubule polymerization	100 μ M	Enzo Life Sciences/ ALX-430-033-M005
Jasplakinolide	Actin filament turnover	8 μ M	BIOMOL Feinchemikalien/ AG- CN2-0037-C050
Latrunculin A	Actin filament polymerization	2 μ M	GmbH/ 10010630
Rhosin	Rho-GTPase activity	200 μ M	Merck Millipore/ 555460
Y16	Rho-GTPase activity	50 μ M	Sigma Aldrich/ SML0873
Rockout	Rho-kinase activity	125 μ M	Santa Cruz Biotechnology/ sc- 203237
ML-7	MLCK activity	250 μ M	Enzo Life Sciences/ BML-EI197-0010
CK-666	Arp2/3-dependent actin nucleation	200 μ M	Merck Millipore/ 182515
SMIFH2	Formin-dependent actin nucleation	10 μ M	Merck Millipore/ 344092

Supplementary Table 2. List of cytoskeleton inhibitors.

Experiment	Number of embryos (N)		Number of cells (n)		Statistical test	Figure
	Hindbrain	Retina	Hindbrain	Retina		
MSD	5	10	13	15	-	Suppl. 1a
Migration starting points (variance)	5	10	13	15	F test	1e
Nuclear velocity – aspect ratio cross-correlation	4	10	13	13	Wilcoxon signed-rank	2h
Fluctuation frequencies (velocity, aspect ratio, basal actin)	-	3	-	4	Mann Whitney	Suppl. 2c
Nuclear velocity, aspect ratio, basal actin cross-correlation	-	3	-	4	-	3e
DMSO control (Rockout)	6	5	131	105	Mann Whitney	4a, d
Rockout live treatment	6	10	250	141	Mann Whitney	4b, d
DMSO control (SMIFH2)	4	8	18	61	Mann Whitney	4e
SMIFH2 live treatment	4	10	23	57	Mann Whitney	4c, e
Unaffected Rockout live treatment	2	-	-	-	-	-
Unaffected SMIFH2 live treatment	-	16	-	-	-	-

Supplementary Table 3. Number of embryos and cells used in the analysis comparing different parameters in hindbrain and retina.

Experiment	Number of embryos (N)				Number of cells (n)				Statistical test	Figure
	HB	R	MHBS	MHBC	HB	R	MHBS	MHBC		
Cell length	5	10	5	7	13	15	6	8	Mann Whitney	Table 2
Apical-to-basal footprint ratio	4	4	4	7	6	5	5	7	Mann Whitney	Table 2
Duration of apical migration (min)	5	10	4	7	13	15	5	8	Mann Whitney	Table 1, 2
Mean instantaneous velocity ($\mu\text{m}/\text{min}$)	5	10	4	7	13	15	5	8	Mann Whitney	Table 1, 2
Basal-to-apical distribution profiles	7	6	10	8	-	-	-	-	-	5a, b, d, e
Nuclear trajectories	5	10	4	7	13	15	5	8	-	1c, d, 5f
Directionality ratio	5	10	4	7	13	15	5	8	-	1f, 5g
Normalized nuclear aspect ratio	4	10	5	5	13	13	6	6	Mann Whitney	2g, Suppl. 1c, 5h

Supplementary Table 4. Number of embryos and cells used in the analysis comparing different parameters in hindbrain, retina, MHBS, and MHBC.

Representative data	Number of instances observed		Figure
	Hindbrain	Retina	
Lamin B1, Lamin A/C staining	3	3	2a
Nuclear deformations (LAP2b)	-	3	2b
Nuclear deformations upon laser ablation	1	1	2c
Perturbed apical migration upon LmnA overexpression	-	3	2e
Actin distribution in single G2 cells	3	4	3a
Basal actin profile	1	1	3b'
Basal actin fluctuations	-	3	3c'
DN-Rok2-EGFP	5	10	3f
Fmnl3 Δ C-EGFP	14	19	3g
Fmnl3-EGFP distribution	-	3	3h
Myosin distribution in single G2 cells	5	3	Suppl. 2b
N-WASP-CA-mKate2	15	11	Suppl. 4b
Fmnl3 in situ hybridization	-	2 independent experiments	Suppl. 4c

Supplementary Table 5. Number of instances representative observations were made.